

High-Fidelity Aerostructural Optimization with Integrated Geometry Parameterization and Mesh Movement

Zimi J. Zhang*, Shahriar Khosravi† and David W. Zingg‡

Institute for Aerospace Studies, University of Toronto

4925 Dufferin Street, Toronto, Ontario, M3H 5T6, Canada

This paper extends previous work on the integrated geometry parameterization and mesh movement strategy for aerodynamic shape optimization to high-fidelity aerostructural optimization based on steady analysis. The proposed approach allows for automatic and efficient grid movement resulting in high quality aerodynamic meshes in response to optimization shape changes and structural deflections. It is also integrated with a surface geometry parameterization that analytically describes the outer mold line at any point with a compact yet flexible set of parameters. A novel structural mesh movement algorithm has been developed, so that any jig shape changes described by the geometry parameterization can be consistently translated to the internal structures. Other components of this framework include an aerodynamic solver capable of three-dimensional inviscid and viscous flow analysis and a finite-element code for structural analysis. The aerodynamic and structural analysis modules are coupled to the linear elasticity mesh movement equations in a three-field formulation of the aerostructural problem. Gradients are computed using an augmented three-field coupled adjoint approach. Both the analysis and the adjoint problems are solved using a partitioned block Gauss-Seidel method. Results obtained by aerostructural analysis are validated with static experimental data from the HIGH REynolds Number Aero-Structural Dynamics (HIRENASD) Project. Capabilities of the framework are demonstrated through the analysis of a flexible C-wing that is created from a planar wing using the integrated geometry parameterization and mesh movement. Finally, an inviscid transonic wing sweep optimization study involving a large number of design variables demonstrates the ability of the methodology to capture the fundamental tradeoff between drag and weight.

Nomenclature

AoA	Angle of attack	\mathbf{G}	Vector containing all nodes on the aerodynamic computational grid
\mathbf{b}	Vector of control point coordinates for the deflected geometry	\mathbf{G}_{J_s}	Coordinates of surface grid nodes on the jig shape
\mathbf{b}_J	Vector of control point coordinates for the undeflected geometry	$\tilde{\mathbf{G}}_{\Delta_s}$	Vector describing the exact displaced aerodynamic surface
\mathbf{b}_{Δ}	Difference in control point coordinates between deflected and undeflected geometries	\mathcal{J}	Objective function
\mathbf{b}_s	Coordinates of surface control points describing the deflected geometry	\mathcal{J}_A	Aerodynamic functional
\mathbf{B}	Coordinates of a single control point	\mathcal{J}_S	Structural functional
\mathbf{f}_A	Surface traction on the aerodynamic surface	\mathbf{K}_M	Stiffness matrix for the mesh equation
\mathbf{f}_M	Force vector in the mesh equation	\mathbf{K}_S	Stiffness matrix for the structural equation
\mathbf{f}_S	Force vector in the structural equation	KS	Kreisselmeier-Steinhauser function for stress aggregation
		\mathcal{L}	Lagrangian function

*Ph.D. Candidate, AIAA Student Member, jenmyzm.zhang@utoronto.ca

†Ph.D. Candidate, AIAA Student Member, shahriar.khosravi@mail.utoronto.ca

‡Professor and Director, Canada Research Chair in Computational Aerodynamics and Environmentally Friendly Aircraft Design, J. Armand Bombardier Foundation Chair in Aerospace Flight, Associate Fellow AIAA, dwz@oddjob.utias.utoronto.ca

\mathbf{M}_S	Vector containing all nodes on the structural mesh/model	\mathbf{v}_S	Structural design variables
\mathcal{N}	B-spline basis functions	ϵ_A	Convergence tolerance for the aerodynamic subproblem
\mathbf{q}	Aerodynamic state vector	ϵ_M	Convergence tolerance for the mesh subproblem
\mathbf{r}	Rigid link vector	ϵ_S	Convergence tolerance for the structural subproblem
\mathbf{R}_{AS}	Aerostructural residual vector	ϵ_{AS}	Convergence tolerance for the aerostructural analysis
\mathbf{R}_A	Aerodynamic residual vector	Ψ_A	Aerodynamic adjoint vector
\mathbf{R}_S	Structural residual vector	$\Psi_{M\Delta}$	Mesh adjoint vector corresponding to the flying shape
$\mathbf{R}_{M\Delta}$	Mesh residual vector for the deflected shape	Ψ_{MJ}	Mesh adjoint vector corresponding to the jig shape
\mathbf{R}_{MJ}	Mesh residual vector for the jig shape	Ψ_S	Structural adjoint vector
\mathbf{u}	Structural state vector	ξ, η, ζ	Parametric coordinates
\mathbf{u}_A	Changes in the aerodynamic surface coordinates due to structural deflections		
\mathbf{v}	Design variables		
\mathbf{v}_A	Aerodynamic design variables		
\mathbf{v}_G	Geometric design variables		

I. Introduction

To sustain rapid growth of the aviation industry under the pressure of rising fuel costs and increasing environmental concern for greenhouse gas emissions, future-generation aircraft must be substantially more fuel efficient.^{1,2,3,4} Conventional tube-and-wing designs are highly optimized and therefore offer limited room for further improvements. In order to achieve the required amount of efficiency gain, unconventional design options must be explored.⁵ This poses a challenge with the traditional cut-and-try approach to aircraft design, which relies heavily on the knowledge and experience of the designer. However, past experience is not available for unconventional configurations. This challenge is being gradually overcome with numerical optimization. More specifically, numerical optimization based on high-fidelity aerodynamic analysis has become increasingly accessible due to more efficient numerical methods and powerful high-performance computing facilities. Although computationally more expensive than low-fidelity models, high-fidelity aerodynamic analysis accurately captures the physics of the flow in regions where low-fidelity models are invalid.

Realistic design problems often involve hundreds and sometimes thousands of design variables. This, together with the cost of large-scale high-fidelity calculations, makes gradient-based optimization methods the preferred option.⁶ The cost of optimization can be further reduced by the use of adjoint methods, where the cost of gradient calculation is almost independent of the number of design variables.^{7,8} These gradients are used by a numerical optimizer to find the optimal set of design parameters. High-fidelity aerodynamic optimization is especially valuable when exploring unconventional design concepts, because a more realistic early assessment can significantly speed up the design cycle and avoid unnecessary investments.

Aerodynamic shape optimization has revealed many promising design concepts that lead to reductions in drag.^{9,10} What remains an interesting and important question is how much these benefits are offset by the possible increase in structural weight. Some recent applications of high-fidelity aerodynamic optimization have included simplified weight models.^{11,12,13,14} However, the tradeoff between drag and weight is more accurately captured with full stress analysis based on aerodynamic loading. High-fidelity aerostructural analysis allows aerodynamic performance to be evaluated at the correct flying shape by computing the structural deflections under the aerodynamic loads. It also provides more accurate indication of possible structural failure, reducing the reliance on artificial geometric constraints that can steer the optimizer away from finding the most efficient design.¹⁵ Furthermore, sequential design cycles, which iterate between pure aerodynamic and structural optimizations, do not guarantee convergence to the true aerostructural optimum.¹⁵ Therefore, optimization based on tightly integrated high-fidelity aerostructural analysis is an important step towards taking full advantage of numerical optimization. Development of such a framework for design exploration of unconventional aircraft is the focus of this paper.

In order to enable shape optimization, the optimizer needs a way to manipulate the geometry. For gradient-based optimization specifically, analytical sensitivities of the geometry with respect to design variables need to be readily available.^{16,17} CAD-free approaches are popular for this reason. The effectiveness of a CAD-free approach is dictated by the choice of geometry parameterization. An appropriate geometry parameterization allows a compact set of design variables to be defined with sufficient flexibility to develop design features of interest to the designer. In the context of aerostructural optimization, shape changes across

disciplines must also be consistently parameterized to maintain the accuracy of the analysis.¹⁸ Moreover, design shape changes cannot be analyzed without efficient and robust mesh movement algorithms to deform the aerodynamic and structural domains. The aerodynamic domain undergoes further deformation during an aerostructural analysis due to structural deflections. This stems from the fact that the aerodynamic analysis uses an Eulerian formulation. An efficient aerodynamic mesh movement algorithm that is capable of handling large geometry changes is hence essential. In contrast, the structural analysis uses a Lagrangian formulation. Therefore, structural mesh movement is only executed once per design cycle. However, it must preserve the quality of the structural components, such as ribs and spars, modeled in high-fidelity analysis.

Various high-fidelity aerostructural optimization methodologies have been described in the literature, which took different approaches in addressing the above challenges in geometry parameterization and mesh movement. Maute *et al.*¹⁹ adopted a three-field formulation for the aerostructural problem. An equation governing the states of the aerodynamic grid based on a spring analogy was coupled to the Euler equations and a linear structural analysis. Maute *et al.*¹⁹ further discussed the three-field coupled adjoint approach for the gradient calculations. The methodology described was applied to the optimization of a wing with a detailed finite-element model. A small number of geometric design variables were defined based on a Coons element.¹⁹ Barcelos *et al.*²⁰ later extended this work to include the Navier-Stokes equations for laminar and turbulent flows. Reuther *et al.*¹⁵ and Martins *et al.*^{21,22} used a more sophisticated outer mold line geometry database as an interface to the optimizer and between the disciplines. The aerodynamic mesh was deformed by an algebraic warping algorithm which does not appear explicitly in the equations of state. Martins *et al.*²² also detailed the corresponding coupled adjoint problem. The design framework was later applied to the optimization of a supersonic business jet based on the Euler equations and a linear finite-element analysis of the structures.²¹ Kenway *et al.*²³ present a parallel scalable high-fidelity aerostructural optimization framework based on the Euler equations and a linear finite-element model capable of solving problems with a large number of design variables and unknowns. They use a free-form-deformation (FFD) technique to parameterize the outer mold line and the internal structure, and a hybrid linear elasticity mesh movement with algebraic warping to move the aerodynamic grid. The described framework is used in the optimization of a NASA Common Research Model (CRM) wing-body-tail configuration.²⁴ In a recent publication, Kenway *et al.*²⁵ perform aerostructural optimization studies based on the Reynolds-Averaged Navier-Stokes equations with the CRM geometry.

The framework presented in this paper uses the integrated geometry parameterization and mesh movement technique proposed by Hicken and Zingg¹⁶ for aerodynamic shape optimization. This approach parameterizes the aerodynamic volume grid by B-spline tensor volumes. Control points on the surface of the geometry provide an efficient means for the optimizer to parameterize and control the geometry with a high degree of flexibility. The physical relationship between the B-spline surface control points and the underlying geometry also allows for intuitive and specific control over local features of the design. The B-spline surface control points can be used as design variables.^{16,9,26,13} An alternative geometric design variable definition via a two-level FFD method has also been described and used.^{17,10} The approximation power of piecewise smooth B-spline surface patches allow complex geometries to be analytically represented and maintained throughout optimization. The initial and optimized geometries are therefore always independent of the mesh used to approximate them. This is an advantage to this approach over other CAD-free approaches where the description of the geometry is discrete and may be altered with mesh refinement. The analytical geometry description may also be used for other important purposes such as rigorous mesh refinement studies and adaptive gridding. The geometry parameterization is tightly integrated with a linear elasticity mesh movement algorithm, so that the quality of the initial grid is maintained in the presence of large shape changes. The integrated geometry parameterization and mesh movement technique has been successfully applied to numerous aerodynamic shape optimization problems involving substantial geometry changes.^{16,9,26,13,17,10}

In its extensions to aerostructural application, the integrated geometry parameterization and mesh movement will parameterize both the undeflected aerodynamic geometry and the flying shape. The proposed aerostructural optimization methodology will be presented in rest of this paper. Section II will start by providing an overview of the high-fidelity aerostructural optimization problem. A more detailed description of the integrated geometry parameterization and mesh movement technique will follow in Section III. A new structural mesh movement method that allows the internal structure to be reshaped according to the geometry parameterization will also be introduced. The proposed methodology uses a three-field formulation similar to that in Maute *et al.*,¹⁹ where the B-spline control grid coordinates are treated as independent state

variables in the aerostructural equation and the adjoint formulation. This will be explained further in Section IV with the introduction of the steady state aerostructural problem. Sensitivity calculations using the coupled adjoint approach will be included in Section V. Finally, results from the validation and application of the proposed framework can be found in Sections VI and VII.

II. Aerostructural Optimization Problem Overview

An aerostructural optimization problem seeks to minimize an objective function, \mathcal{J} , with respect to a set of design variables, \mathbf{v} . The optimization is subject to a partial differential equation constraint, namely the discrete steady aerostructural equations, \mathbf{R}_{AS} . The optimization may also be subject to a number of equality constraints, C_{eq} , and inequality constraints, C_{in} , which may be linear or nonlinear. The optimization problem can be summarized as follows:

$$\min_{\mathbf{v}} \mathcal{J}(\mathbf{v}, [\mathbf{q}, \mathbf{u}, \mathbf{b}_{\Delta}]^T), \quad \mathbf{R}_{AS}(\mathbf{v}, [\mathbf{q}, \mathbf{u}, \mathbf{b}_{\Delta}]^T) = 0, \quad \text{s.t.} \quad \begin{aligned} C_{eq,i}(\mathbf{v}, [\mathbf{q}, \mathbf{u}, \mathbf{b}_{\Delta}]^T) &= 0, & i &= 1, \dots, n_{eq} \\ l_j \leq C_{in,j}(\mathbf{v}, [\mathbf{q}, \mathbf{u}, \mathbf{b}_{\Delta}]^T) &\leq u_j, & j &= 1, \dots, n_{in} \end{aligned} \quad (1)$$

The lower and upper bounds for the j^{th} inequality constraint are given by l_j and u_j , respectively. The aerostructural state variables are given by $[\mathbf{q}, \mathbf{u}, \mathbf{b}_{\Delta}]^T$, where \mathbf{q} is the flow state, \mathbf{u} is the structural state, and \mathbf{b}_{Δ} is the aerodynamic mesh state due to structural deflections. The state variables depend on \mathbf{v} through aerostructural analysis, which solves $\mathbf{R}_{AS} = 0$. The design variables are categorized into geometric (i.e. \mathbf{v}_G), aerodynamic (i.e. \mathbf{v}_A), and structural (i.e. \mathbf{v}_S) design variables, which specify the geometry, flow conditions, and structural properties for the analysis, respectively. More details regarding aerostructural analysis are discussed in Section IV. The optimization problem is solved using SNOPT,²⁷ which is a gradient-based sequential quadratic programming (SQP) algorithm that is well-suited for large-scale, nonlinear optimization problems. A third-party Python interface to SNOPT²⁸ is used with some modifications for this work.

Aerostructural analysis allows multidisciplinary objectives, including both aerodynamic and structural functionals, to be evaluated and minimized. Examples of objective functions include range, fuel burn, or some linear combination of weight and drag for more specific tradeoff studies. A lift constraint is included for each load condition considered. To avoid structural failure, the stresses on all structural elements must be below the yield stress of the material. The Kreisselmeier-Steinhauser (KS)^{29,30,31} function is used to aggregate the element stress constraints into a smaller number of structural constraints, so that the coupled adjoint method remains effective. Geometric and other constraints may also be added. An example of an aerodynamic design variable is the angle of attack (AoA). Structural design variables may include component thickness of the structures. This paper uses the coordinates of the surface B-spline control points as geometric design variables, more of which will be discussed in Section III.

Unsteady aeroelastic phenomena such as flutter, and dynamic structural failure modes such as buckling, are not currently considered. However, the purpose of this work is not to accurately capture all realistic aspects of practical aircraft design, but to explore methodologies which can effectively capture the important tradeoffs between weight and drag. Modeling static aerostructural coupling is sufficient for this purpose, and it will serve as an important step towards incorporating unsteady and dynamic effects in the future.

III. Integrated Geometry Parameterization and Mesh Movement

III.A. Geometry Parameterization

The integrated geometry parameterization and mesh movement technique uses a B-spline tensor-product volume which maps a point from parametric space, $D = \{\boldsymbol{\xi} = (\xi, \eta, \zeta) \in \mathbb{R}^3 | \xi, \eta, \zeta \in [0, 1]\}$, to physical space, $P \subset \mathbb{R}^3$, according to the following mathematical relationship:¹⁶

$$\mathbf{x}(\boldsymbol{\xi}) = \sum_{i=1}^{N_i} \sum_{j=1}^{N_j} \sum_{k=1}^{N_k} \mathbf{B}_{ijk} \mathcal{N}_i^{(p)}(\xi) \mathcal{N}_j^{(p)}(\eta) \mathcal{N}_k^{(p)}(\zeta), \quad (2)$$

where \mathbf{B}_{ijk} are the coordinates of the de Boor control points, and $\mathcal{N}_i^{(p)}(\xi)$, $\mathcal{N}_j^{(p)}(\eta)$, $\mathcal{N}_k^{(p)}(\zeta)$ are B-spline basis functions of order p in each parametric coordinate direction. An entire aerodynamic volume grid can be fully described by a grid of B-spline control points, given that the parametric coordinates of each aerodynamic

grid node are known. This allows the aerodynamic grid to be parameterized and modified via changes to the B-spline control volume. The number of nodes in the control volume is typically about two orders of magnitude fewer than the number in the aerodynamic grid.

In order to tailor the B-spline basis to different edges of an aerodynamic geometry, Hicken and Zingg¹⁶ generalized the basis functions to incorporate spatially varying knots, or curved knot lines. As an example, basis functions in the ξ -direction are given by

$$\mathcal{N}_i^{(1)}(\xi; \eta, \zeta) = \begin{cases} 1 & \text{if } T_i(\eta, \zeta) \leq \xi < T_{i+1}(\eta, \zeta) \\ 0 & \text{otherwise} \end{cases} \quad (3)$$

$$\mathcal{N}_i^{(p)} = \left(\frac{\xi - T_i(\eta, \zeta)}{T_{i+p-1}(\eta, \zeta) - T_i(\eta, \zeta)} \right) \mathcal{N}_i^{(p-1)}(\xi; \eta, \zeta) + \left(\frac{T_{i+p}(\eta, \zeta) - \xi}{T_{i+p}(\eta, \zeta) - T_{i+1}(\eta, \zeta)} \right) \mathcal{N}_{i+1}^{(p-1)}(\xi; \eta, \zeta),$$

where $T_i(\eta, \zeta)$ are the knot values. Open knot vectors are used such that the first and last p knots of $T_i(\eta, \zeta)$ are forced to be 0 and 1, respectively. The internal knots follow a bilinear distribution such that

$$T_i(\eta, \zeta) = [(1 - \eta)(1 - \zeta)] T_{i,(0,0)} + [\eta(1 - \zeta)] T_{i,(1,0)} + [(1 - \eta)\zeta] T_{i,(0,1)} + [\eta\zeta] T_{i,(1,1)}, \quad (4)$$

where $T_{i,(0,0)}$, $T_{i,(1,0)}$, $T_{i,(0,1)}$ and $T_{i,(1,1)}$ are the i^{th} knot values along the η and ζ edges of the parameter space. The basis functions $\mathcal{N}_j^{(p)}(\eta; \xi, \zeta)$ and $\mathcal{N}_k^{(p)}(\zeta; \xi, \eta)$ can be similarly described.

To parameterize the aerodynamic volume grid with B-splines, parametric coordinates of each grid node are first determined using chord-length parameterization. The edge knot values are chosen to ensure an equal number of nodes within each knot interval, leading to a chord-length-based knot distribution. The initial B-spline control point coordinates are obtained by least-squares fitting of an initial grid. The resulting control volume is a coarse grid with mesh spacing that resembles the original computational grid because of the nature of the knot distribution. This is a characteristic that is exploited in the mesh movement algorithm described later. For the multi-block structured aerodynamic grids used for this work, each block is described by a separate control volume with coincident control points at the block interfaces to ensure continuity.¹⁶ Figure 1 provides an example of a control grid and the corresponding computational grid.

In the present framework, control points on the surface of the geometry, which are represented by blue spheres in Figure 1, are used as design variables. Planform variables like sweep and sectional twist are defined by a combination of linear constraint and control points grouping. Values of the geometric design variables assigned by the optimizer to describe the undeflected outer mold line are denoted by \mathbf{v}_G . During an aerostructural analysis, surface control points are also used to describe the deflected flying shape. Coordinates of the surface control points are given by \mathbf{b}_s , and are functions of \mathbf{v}_G and \mathbf{u} . Section IV describes in more detail how the surface control point coordinates are determined. The displaced surface control mesh directly specifies the boundary conditions for the mesh movement problem described in Section III.B. Extension of this method to parameterize the structural model is described in Section III.C.

III.B. Aerodynamic Mesh Movement

Changes in the B-spline surface control points are propagated to the interior volume via a linear elasticity mesh movement applied to the control grid. Large shape changes are broken into m increments. Given the coordinates of the displaced surface control points, $\mathbf{b}_s^{(i)}$, which defines the force vector, $\mathbf{f}_M^{(i)}$, the vector of control point coordinates, $\mathbf{b}^{(i)}$, is updated by solving¹⁶

$$\mathbf{R}_M^{(i)}(\mathbf{b}^{(i-1)}, \mathbf{b}^{(i)}) = \mathbf{K}_M^{(i)}(\mathbf{b}^{(i-1)})[\mathbf{b}^{(i)} - \mathbf{b}^{(i-1)}] - \mathbf{f}_M^{(i)}(\mathbf{b}_s^{(i)}) = 0, \quad i = 1, \dots, m, \quad (5)$$

where $\mathbf{R}_M^{(i)}$ is the mesh residual and $\mathbf{K}_M^{(i)}$ the stiffness matrix. A spatially-varying Young's modulus is used to preserve the quality of the control grid, which makes $\mathbf{K}_M^{(i)}$ a function of $\mathbf{b}^{(i-1)}$. For clarity, this paper does not treat \mathbf{b}_s as a subset of \mathbf{b} , but rather an input to (5). The solution of (5) is found by a parallel conjugate-gradient method preconditioned by an additive Schwarz method with local Jacobi preconditioning, all of which are available in the PETSc library.³² The new aerodynamic grid is simply re-evaluated according to (2).

Linear elasticity mesh movement is known to be very robust even in the presence of large shape changes. It is much cheaper to apply this method to the control grid as opposed to the full aerodynamic grid. The quality of the aerodynamic grid is nonetheless preserved by the similarity in the relative mesh spacing between

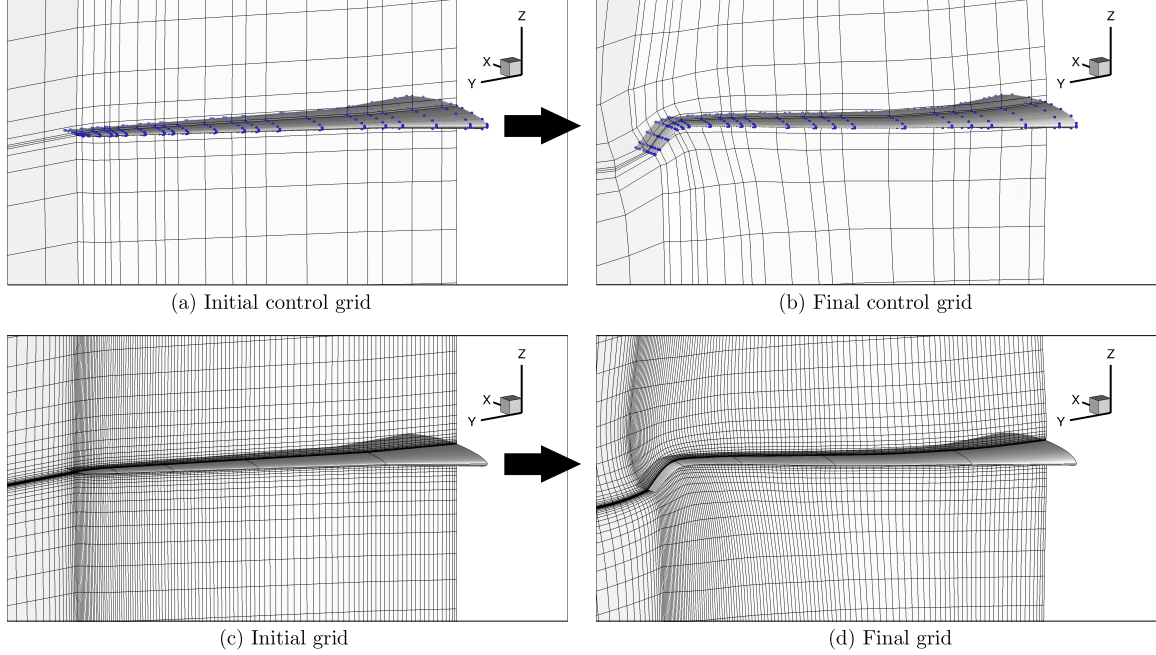


Figure 1: The integrated mesh movement scheme is applied to the control grid in (a) to accomplish a shape change in (b). Surface control points for both geometries are represented by blue spheres. The corresponding initial and final computational grids are shown in (c) and (d), respectively.

the control grid and the aerodynamic grid. Figure 1 illustrates the resulting control grid and computational grid following a mesh movement to obtain a winglet-down geometry.

III.C. Structural Mesh Movement

In the present framework, the structural mesh remains fixed during aerostructural analysis, but shape changes described by the geometric design variables must be translated consistently to the structural model for accurate force and displacement transfer. Parameterization of the detailed internal structure using B-splines would involve a complex arrangement of intersecting parametric surfaces. In contrast, FFD is geometric fidelity independent^{33,18} and therefore remains the most simple and effective way to move the structural mesh. Therefore, a novel surface-based FFD method has been developed which parameterizes the space enclosed between the B-spline surfaces and allows it to act like an FFD volume embedding the structure.

Given a point P on the structural model, the surface-based FFD method begins by associating it with two points U and L , on the upper and lower surfaces of the geometry, respectively. This is illustrated in Figure 2. The coordinates of U and L are given by

$$U(\xi_1, \eta) = \sum_{j=1}^{N_j} \sum_{k=1}^{N_k} \mathcal{N}_j(\xi_1) \mathcal{N}_k(\eta) B_{jkN_m} \quad \text{and} \quad L(\xi_2, \eta) = \sum_{j=1}^{N_j} \sum_{k=1}^{N_k} \mathcal{N}_j(\xi_2) \mathcal{N}_k(\eta) B_{jk1}, \quad (6)$$

where ξ_1 , ξ_2 and η are the chordwise and spanwise parametric coordinates of U and L on the B-spline surfaces, and B_{jkN_m} and B_{jk1} are the corresponding surface control points. The points P , U , and L should be collinear, such that the coordinates of P can be described by a parametric distance ℓ as follows:

$$U(\xi_1, \eta) + \ell [L(\xi_2, \eta) - U(\xi_1, \eta)] - P = 0. \quad (7)$$

Once the appropriate U and L are found for each P at the start of an optimization, ξ_1 , ξ_2 , η and ℓ are fixed and the coordinates of P become a function of the B-spline surface control points. Furthermore, U and L

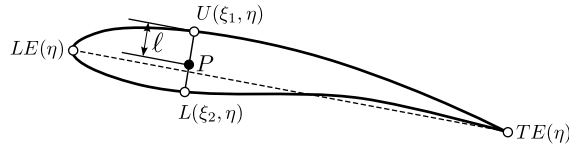


Figure 2: The straight line which associates a structural mesh node, P , with the surfaces of a wing section described by a constant spanwise parametric coordinate η .

are required to have the same η such that P remains in the same spanwise parametric section during shape changes. In order to associate each P with a unique pair of (U, L) , two constraints are defined based on vector dot products:

$$\text{Let: } \begin{cases} \overrightarrow{UP} &= U(\xi_1, \eta) - P \\ \overrightarrow{LP} &= L(\xi_2, \eta) - P \\ \overrightarrow{C} &= TE(\eta) - LE(\eta) \end{cases}, \quad \text{then: } \begin{cases} \overrightarrow{UP} \cdot \overrightarrow{C} &= 0 \\ \overrightarrow{LP} \cdot \overrightarrow{C} &= 0 \end{cases}. \quad (8)$$

Equation (8) requires the line UPL (see Figure 2), along which P is parameterized, to be normal to the chord defined by the leading edge, LE , and trailing edge, TE , of the same η . For most topologies, these constraints ensure that UPL is close to being tangent to the ribs and spars, and is aligned with the direction in which sectional shape changes are defined. This can reduce the amount of unwanted distortion introduced to the structural components during shape changes. The surface-based FFD method is functionally equivalent to forming an FFD control lattice directly from the available B-spline surface control points, but it avoids the potential limitations imposed on the number and distribution of control points on the upper and lower surfaces.

For future extensions to more complex geometries, such as a split-tip wing where a straight line through U , P and L may not exist for all P , (7) and (8) are programmed as a more general minimization problem solved via SQP.³⁴ The current implementation is also capable of handling multiple surface patches. Associating all points on the structural model with the B-spline geometry definition is the most expensive part of this surface-based FFD method. However, it is done only once at the beginning of an optimization, and its cost is still negligible in comparison to the aerostructural optimization problem. Re-evaluation of the new structural geometry involves simple algebraic expressions, so it is extremely efficient. Geometric sensitivities of the structural mesh points with respect to the surface control points are also easy to obtain by the chain rule.

IV. Steady-State Aerostructural Analysis

During aerostructural analysis, the integrated geometry parameterization and mesh movement technique described in Section III is used to obtain the deformed aerodynamic grid due to structural deflections. A three-field formulation is adopted here, where the mesh equation, $\mathbf{R}_{M\Delta}$, is coupled to the aerodynamic equation, \mathbf{R}_A , and the structural equation, \mathbf{R}_S . The aerostructural residual is therefore written as follows:

$$\mathbf{R}_{AS} = \begin{bmatrix} \mathbf{R}_A(\mathbf{q}, \mathbf{b}_\Delta) \\ \mathbf{R}_S(\mathbf{q}, \mathbf{u}, \mathbf{b}_\Delta) \\ \mathbf{R}_{M\Delta}(\mathbf{u}, \mathbf{b}_\Delta) \end{bmatrix}. \quad (9)$$

The mesh equation, $\mathbf{R}_{M\Delta}$, is given by (5) with $\mathbf{b}^{(i)} = \mathbf{b}_J^{(i)} + \mathbf{b}_\Delta^{(i)}$, $j = 1, \dots, m$. To simplify the notation, let $\mathbf{R}_{M\Delta}$ refer to the vector containing all the incremental mesh residuals, i.e. $\mathbf{R}_{M\Delta} = [\mathbf{R}_{M\Delta}^{(1)}, \mathbf{R}_{M\Delta}^{(2)}, \dots, \mathbf{R}_{M\Delta}^{(m)}]^T$. The displaced mesh state, \mathbf{b}_Δ , represents the changes between the B-spline control points for the jig shape, \mathbf{b}_J , and those for the final deflected shape, \mathbf{b} . A simplified notation is also used for \mathbf{b}_Δ , \mathbf{b}_J , and \mathbf{b} , such that the control point coordinates for all increments are expressed as a single vector.

A two-field formulation, which only involves an aerodynamic and a structural equation, assumes an explicit dependence of \mathbf{R}_A on \mathbf{u} , or that $(\partial \mathbf{R}_A / \partial \mathbf{u}) \neq 0$. It can be recovered from (9) by solving $\mathbf{R}_{M\Delta} = 0$ for every change in \mathbf{u} . Evaluating the sensitivities of \mathbf{R}_A with respect to \mathbf{u} also requires the sensitivities of the aerodynamic volume grid, \mathbf{G} , with respect to \mathbf{u} . However, this term cannot be easily obtained for the

mesh movement strategy described in Section III.B, because the mesh nodes are implicitly coupled to the surface control points according to (5). It is therefore more efficient and straightforward to use a three-field formulation.

The present aerostructural framework is constructed over existing aerodynamic, structural and mesh movement modules. The steady-state solution to (9) is obtained via a nonlinear block Gauss-Seidel method, which involves sub-iterations within each module, allowing existing solution routines to be reused. Detailed application of the nonlinear block Gauss-Seidel method is included in Section IV.C, after the aerodynamic and structural modules are first described in Sections IV.A and IV.B.

IV.A. Aerodynamic Analysis

The aerodynamic module is capable of analysis based on both the three-dimensional Euler equations governing inviscid flow³⁵ and the Reynolds-Averaged Navier-Stokes (RANS) equations governing turbulent flow.³⁶ Although the present framework is capable of performing aerostructural analysis based on the RANS equations, it is currently coded for aerstructural optimization based on the Euler equations only. The flow equations are discretized on a multi-block structured mesh using second-order summation-by-parts (SBP) finite-difference operators. The use of simultaneous-approximation terms (SATs) maintains solution accuracy and time stability without requiring grid continuity at block interfaces and boundaries,³⁵ thereby simplifying interface solution coupling and boundary treatments. The discrete steady aerodynamic equation can be written as

$$\mathbf{R}_A(\mathbf{q}, \mathbf{b}_\Delta) = 0. \quad (10)$$

Due to the presence of the displaced mesh state, \mathbf{R}_A does not explicitly depend on \mathbf{u} , but instead depends on \mathbf{b}_Δ through the volume grid, \mathbf{G} . The aerodynamic solver is equipped with a sophisticated algorithm for the solution of (10) during the aerodynamic sub-iterations. The solution process is accelerated by an efficient parallel implicit Newton-Krylov-Schur algorithm. An appropriate initial solution for Newton's method is obtained by pseudo-transient continuation, which involves a first-order Jacobian approximation with a lagged update, and spatially varying time steps.³⁵ Once the solution has converged to a reasonable tolerance, the algorithm switches to an inexact-Newton method. The resulting linear system at every sub-iteration is solved by a flexible variant of the generalized minimal residual (GMRES) method.³⁵ The linear problem is preconditioned by an approximate Schur factorization, where the inverse of the local Schur complement on each process is approximated using the ILU(p) factorization of the local first-order Jacobian.³⁵

IV.B. Structural Analysis

The structural analysis is provided by the Toolkit for the Analysis of Composite Structures (TACS).^{30,37} It is a parallel finite-element code capable of handling composites and materials with geometric nonlinearity, as well as computing design variable sensitivities.^{30,37} For the purpose of this work, the structural components are modeled using second-order mixed interpolation of tensorial components (MITC) shell elements, which are shown to be effective in avoiding shear-locking.³⁷ A linear constitutive relationship is used and geometric nonlinearity is not modeled. The resulting finite-element equation can be written as

$$\mathbf{R}_S(\mathbf{q}, \mathbf{u}, \mathbf{b}_\Delta) = \mathbf{K}_S \mathbf{u} - \mathbf{f}_S(\mathbf{q}, \mathbf{b}_\Delta). \quad (11)$$

The force vector, \mathbf{f}_S , in this case is a result of aerodynamic loading, the magnitude and direction of which are explicit functions of \mathbf{q} and \mathbf{b}_Δ . Equation (11) is solved by GMRES preconditioned by a direct Schur method, where the global Schur complement is factored exactly because the system is often ill-conditioned.^{30,37}

The aerodynamic, structural and mesh equations are coupled by enforcing appropriate boundary conditions at the aerostructural interface. The interface includes nodes on the aeroelastic parts of the aerodynamic surface (e.g. the wing), and structural nodes adjacent to the aerodynamic surface. Specifically, the coupling is achieved by the transfer of forces and displacements through the interface. The present framework uses a rigid link method that is available in TACS.^{22,23} The rigid link vectors are created at the start of optimization, where each aerodynamic node at the interface is paired with the closest point on the structural model. These rigid links allow displacements and forces to be extrapolated between the aerodynamic and structural domains, even though the two grids may not necessarily overlap at the interface. More details regarding this method can be found in Martins *et al.*²² and Kenway *et al.*²³

IV.C. Aerostructural Solution

Before each analysis, surface B-spline control point coordinates are determined from the geometric design variables, \mathbf{v}_G . Control point coordinates for the undeflected geometry, \mathbf{b}_J , are subsequently evaluated by solving (5) with $\mathbf{b}_\Delta = 0$ and $\mathbf{b} = \mathbf{b}_J$. The structural geometry is deformed as described in Section III.C on page 6. The geometric design variables also provide a description of the jig shape geometry, \mathbf{G}_{J_s} , from which deflection is measured during analysis. After determining the aerodynamic and structural design variables, (9) is solved via a nonlinear block Gauss-Seidel method. The solution procedure at the k^{th} block Gauss-Seidel iteration is outlined below:

1. Obtain displacements of the aerodynamic surface, \mathbf{u}_A , based on the structural state from the previous iteration: $\mathbf{u}^{(k-1)} \rightarrow \mathbf{u}_A^{(k)}$;
2. Calculate the exact displaced surface: $\tilde{\mathbf{G}}_{\Delta_s}^{(k)} = \mathbf{G}_{J_s} + \mathbf{u}_A^{(k)}$;
3. Find surface control point coordinates, \mathbf{b}_s which best describe the displaced surface by least-squares fitting: $\tilde{\mathbf{G}}_{\Delta_s}^{(k)} \rightarrow \mathbf{b}_s^{(k)}$;
4. Update \mathbf{b}_Δ by solving the mesh equation until $\|\mathbf{R}_{M\Delta}(\mathbf{b}_s^{(k)}, \mathbf{b}_\Delta^{(k)})\|_2 \leq \epsilon_M \|\mathbf{R}_{M\Delta}(\mathbf{b}_s^{(k)}, \mathbf{b}_\Delta^{(k-1)})\|_2$;
5. Evaluate the aerodynamic volume grid, \mathbf{G} , for the deflected shape: $\mathbf{b}_J + \mathbf{b}_\Delta^{(k)} \rightarrow \mathbf{G}^{(k)}$;
6. Update \mathbf{q} by solving the aerodynamic equation until $\|\mathbf{R}_A(\mathbf{G}^{(k)}, \mathbf{q}^{(k)})\|_2 \leq \epsilon_A \|\mathbf{R}_A(\mathbf{G}^{(k)}, \mathbf{q}^{(k-1)})\|_2$;
7. Calculate the aerodynamic surface traction, \mathbf{f}_A , on the new aerodynamic grid: $\mathbf{q}^{(k)}, \mathbf{G}^{(k)} \rightarrow \mathbf{f}_A^{(k)}$;
8. Transfer the aerodynamic forces to the structures: $\mathbf{f}_A^{(k)} \rightarrow \mathbf{f}_S^{(k)}$;
9. Solve the structural equation until $\|\mathbf{R}_S(\mathbf{f}_S^{(k)}, \mathbf{u}^{(k-1)} + \Delta\mathbf{u}^{(k)})\|_2 \leq \epsilon_S \|\mathbf{R}_S(\mathbf{f}_S^{(k)}, \mathbf{u}^{(k-1)})\|_2$ for an update $\Delta\mathbf{u}^{(k)}$, then evaluate the new \mathbf{u} using Aitken acceleration.^{38,23}

The parameters ϵ_M , ϵ_A and ϵ_S determine how tightly each sub-problem is solved, and are typically set to 10^{-1} , 10^{-6} , and 10^{-3} , respectively. The Aitken acceleration used during the structural update is an adaptive under-relaxation algorithm. It has been shown to improve the stability and convergence of the nonlinear block Gauss-Seidel method.²³ Lastly, it is necessary to clarify that $\tilde{\mathbf{G}}_{\Delta_s}$ is not equal to \mathbf{G} on the surface due to fitting error. Although the original force and displacement transfer scheme is consistent and conservative,^{22,23,24} the current implementation no longer guarantees conservation. Some studies on the the possible implications are included in Section VI.A on page 12. On the other hand, the grid smoothing introduced by the B-spline fitting has led to better convergence behaviors in some cases, so it may in fact be desirable. Continued investigations in the future are necessary to draw a definite conclusion.

The stopping criterion for the nonlinear block Gauss-Seidel iterations examines the residual norm of each equation separately to account for differences in scaling.^{30,19} The solution is considered converged when the starting residual norms for all sub-problems have been sufficiently reduced, i.e.

$$\begin{aligned} \|\mathbf{R}_M(\mathbf{u}^{(k-1)}, \mathbf{b}^{(k-1)})\|_2 &< \epsilon_{AS} \|\mathbf{R}_M(\mathbf{u}^{(0)}, \mathbf{b}^{(0)})\|_2 \\ \|\mathbf{R}_A(\mathbf{q}^{(k-1)}, \mathbf{b}^{(k)})\|_2 &< \epsilon_{AS} \|\mathbf{R}_A(\mathbf{q}^{(0)}, \mathbf{b}^{(0)})\|_2 \\ \|\mathbf{R}_S(\mathbf{q}^{(k)}, \mathbf{u}^{(k-1)}, \mathbf{b}^{(k)})\|_2 &< \epsilon_{AS} \|\mathbf{R}_S(\mathbf{q}^{(0)}, \mathbf{u}^{(0)}, \mathbf{b}^{(0)})\|_2. \end{aligned} \quad (12)$$

The relative tolerance for the aerostructural problem, ϵ_{AS} , is typically set to 10^{-7} .

V. Sensitivity Evaluation by the Coupled Adjoint Method

The coupled adjoint formulation has been previously described by various authors.^{22,19} It is presented here for the current aerostructural optimization methodology, using the method of Lagrange multipliers adopted by Hicken and Zingg¹⁶ for aerodynamic optimization. Consider the optimization of a functional \mathcal{J} ,

subject to $\mathbf{R}_{AS} = 0$ and $\mathbf{R}_{MJ} = 0$, where \mathbf{R}_{MJ} is the aerodynamic mesh equation for the jig shape. The Lagrangian function for this problem is

$$\mathcal{L} = \mathcal{J}(\mathbf{v}, \mathbf{b}_J, [\mathbf{q}, \mathbf{u}, \mathbf{b}_\Delta]^T) + \Psi_{MJ}^T \mathbf{R}_{MJ}(\mathbf{v}, \mathbf{b}_J) + \begin{bmatrix} \Psi_A^T & \Psi_S^T & \Psi_{M\Delta}^T \end{bmatrix} \begin{bmatrix} \mathbf{R}_A(\mathbf{v}, \mathbf{b}_J, [\mathbf{q}, \mathbf{b}_\Delta]^T) \\ \mathbf{R}_S(\mathbf{v}, \mathbf{b}_J, [\mathbf{q}, \mathbf{u}, \mathbf{b}_\Delta]^T) \\ \mathbf{R}_{M\Delta}(\mathbf{v}, \mathbf{b}_J, [\mathbf{u}, \mathbf{b}_\Delta]^T) \end{bmatrix}, \quad (13)$$

where Ψ_{MJ} , Ψ_A , Ψ_S and $\Psi_{M\Delta}$ are the Lagrange multipliers. The aerostructural residual and state variables are expanded into $\mathbf{R}_{AS} = [\mathbf{R}_A, \mathbf{R}_S, \mathbf{R}_{M\Delta}]^T$ and $[\mathbf{q}, \mathbf{u}, \mathbf{b}_\Delta]^T$, respectively, so that individual derivative terms can be discussed separately. However, brackets are kept around the aerostructural residual and the aerostructural state to remind the readers that these terms are in fact parts of a single term and should be treated as one. The first-order optimality conditions require that the partial derivatives of \mathcal{L} with respect to \mathbf{b}_J and $[\mathbf{q}, \mathbf{u}, \mathbf{b}_\Delta]^T$ be zero:

$$\begin{aligned} \frac{\partial \mathcal{L}}{\partial \mathbf{b}_J} = 0 &\Rightarrow \Psi_{MJ}^T \frac{\partial \mathbf{R}_{MJ}}{\partial \mathbf{b}_J} + \begin{bmatrix} \Psi_A^T & \Psi_S^T & \Psi_{M\Delta}^T \end{bmatrix} \left(\frac{\partial}{\partial \mathbf{b}_J} \begin{bmatrix} \mathbf{R}_A \\ \mathbf{R}_S \\ \mathbf{R}_{M\Delta} \end{bmatrix} \right) = -\frac{\partial \mathcal{J}}{\partial \mathbf{b}_J}, \quad (14) \\ \frac{\partial \mathcal{L}}{\partial [\mathbf{q}, \mathbf{u}, \mathbf{b}_\Delta]^T} = 0 &\Rightarrow \begin{bmatrix} \Psi_A^T & \Psi_S^T & \Psi_{M\Delta}^T \end{bmatrix} \left(\frac{\partial}{\partial [\mathbf{q}, \mathbf{u}, \mathbf{b}_\Delta]^T} \begin{bmatrix} \mathbf{R}_A \\ \mathbf{R}_S \\ \mathbf{R}_{M\Delta} \end{bmatrix} \right) = -\frac{\partial \mathcal{J}}{\partial [\mathbf{q}, \mathbf{u}, \mathbf{b}_\Delta]^T}. \end{aligned}$$

Taking the transpose of the above equations leads to the following linear system :

$$\begin{bmatrix} \frac{\partial \mathbf{R}_{MJ}}{\partial \mathbf{b}_J}^T & \frac{\partial \mathbf{R}_A}{\partial \mathbf{b}_J}^T & \frac{\partial \mathbf{R}_S}{\partial \mathbf{b}_J}^T & \frac{\partial \mathbf{R}_{M\Delta}}{\partial \mathbf{b}_J}^T \\ \frac{\partial \mathbf{R}_A}{\partial \mathbf{q}}^T & \frac{\partial \mathbf{R}_S}{\partial \mathbf{q}}^T & 0 & 0 \\ 0 & 0 & \frac{\partial \mathbf{R}_S}{\partial \mathbf{u}}^T & \frac{\partial \mathbf{R}_{M\Delta}}{\partial \mathbf{u}}^T \\ \frac{\partial \mathbf{R}_A}{\partial \mathbf{b}_\Delta}^T & \frac{\partial \mathbf{R}_S}{\partial \mathbf{b}_\Delta}^T & \frac{\partial \mathbf{R}_{M\Delta}}{\partial \mathbf{b}_\Delta}^T & 0 \end{bmatrix} \begin{bmatrix} \Psi_{MJ} \\ \Psi_A \\ \Psi_S \\ \Psi_{M\Delta} \end{bmatrix} = \begin{bmatrix} -\frac{\partial \mathcal{J}}{\partial \mathbf{b}_J}^T \\ -\frac{\partial \mathcal{J}}{\partial \mathbf{q}}^T \\ -\frac{\partial \mathcal{J}}{\partial \mathbf{u}}^T \\ -\frac{\partial \mathcal{J}}{\partial \mathbf{b}_\Delta}^T \end{bmatrix}. \quad (15)$$

Equation (15) is solved by first solving for $[\Psi_A, \Psi_S, \Psi_{M\Delta}]^T$, which are coupled by the transposed aerostructural Jacobian, and then solving for Ψ_{MJ} . However, recall from Section IV on page 7 that $\mathbf{b} = \mathbf{b}_J + \mathbf{b}_\Delta$. Hence the following is true:

$$\frac{\partial}{\partial \mathbf{b}_\Delta} \begin{bmatrix} \mathbf{R}_A \\ \mathbf{R}_S \\ \mathbf{R}_{M\Delta} \end{bmatrix} = \frac{\partial}{\partial \mathbf{b}_J} \begin{bmatrix} \mathbf{R}_A \\ \mathbf{R}_S \\ \mathbf{R}_{M\Delta} \end{bmatrix}, \quad \text{and} \quad \frac{\partial \mathcal{J}}{\partial \mathbf{b}_\Delta} = \frac{\partial \mathcal{J}}{\partial \mathbf{b}_J}. \quad (16)$$

Due to the last row in the coupled adjoint system, the first row of (15) reduces to

$$\begin{aligned} \frac{\partial \mathbf{R}_{MJ}}{\partial \mathbf{b}_J}^T \Psi_{MJ} &= -\frac{\partial \mathcal{J}}{\partial \mathbf{b}_J}^T - \frac{\partial \mathbf{R}_A}{\partial \mathbf{b}_J}^T \Psi_A - \frac{\partial \mathbf{R}_S}{\partial \mathbf{b}_J}^T \Psi_S - \frac{\partial \mathbf{R}_{M\Delta}}{\partial \mathbf{b}_J}^T \Psi_{M\Delta} \Rightarrow \Psi_{MJ} = 0. \quad (17) \\ &= 0 \end{aligned}$$

The derivation is completed by taking the partial derivative of \mathcal{L} with respect to \mathbf{v} :

$$\mathcal{G} = \frac{\partial \mathcal{J}}{\partial \mathbf{v}} + \frac{\partial \mathbf{R}_{MJ}}{\partial \mathbf{v}}^T \Psi_{MJ} + \frac{\partial \mathbf{R}_A}{\partial \mathbf{v}}^T \Psi_A + \frac{\partial \mathbf{R}_S}{\partial \mathbf{v}}^T \Psi_S + \frac{\partial \mathbf{R}_{M\Delta}}{\partial \mathbf{v}}^T \Psi_{M\Delta}, \quad (18)$$

which is the expression for the total gradient of \mathcal{J} with respect to the design variables. The Lagrange multipliers used here are equivalent to the adjoint variables.

Solution to the coupled adjoint problem in (15) is computed via a linear block Gauss-Seidel method. At each iteration k , the following equations are solved in sequence:

$$\frac{\partial \mathbf{R}_A}{\partial \mathbf{q}}^T \Psi_A^{(k+1)} = -\frac{\partial \mathcal{J}^T}{\partial \mathbf{q}} - \frac{\partial \mathbf{R}_S}{\partial \mathbf{q}}^T \Psi_S^{(k)} \quad (19)$$

$$\mathbf{K}_S \Psi_S^{(k+1)} = -\frac{\partial \mathcal{J}^T}{\partial \mathbf{u}} - \frac{\partial \mathbf{R}_{M\Delta}}{\partial \mathbf{u}}^T \Psi_{M\Delta}^{(k)} \quad (20)$$

$$\frac{\partial \mathbf{R}_{M\Delta}}{\partial \mathbf{b}_\Delta}^T \Psi_{M\Delta}^{(k+1)} = -\frac{\partial \mathcal{J}^T}{\partial \mathbf{b}_\Delta} - \frac{\partial \mathbf{R}_A}{\partial \mathbf{b}_\Delta}^T \Psi_A^{(k+1)} - \frac{\partial \mathbf{R}_S}{\partial \mathbf{b}_\Delta}^T \Psi_S^{(k+1)}. \quad (21)$$

Implementation of the sensitivity terms in (19–21) follows the work of Kenway *et al.*²³ Appropriate modifications have been introduced due to the additional mesh state and mesh equation. To facilitate further discussions on the gradient calculations, it is convenient to first distinguish between aerodynamic functionals, denoted by \mathcal{J}_A , and structural functionals, denoted by \mathcal{J}_S . An aerodynamic functional, such as lift and drag, does not depend explicitly on structural variables. Conversely, structural functionals, such as mass and the KS functions, do not depend explicitly on aerodynamic variables. Sensitivities of \mathcal{J}_A and \mathcal{J}_S can be combined to obtain sensitivities of composite functionals, such as range.

Equation (19) is solved by a flexible variant of GCROT proposed by Hicken and Zingg.¹⁶ The transposed aerodynamic Jacobian, $(\partial \mathbf{R}_A / \partial \mathbf{q})^T$, is evaluated by a combination of analytical and complex-step differentiation, and is subsequently stored. On the right-hand side, $(\partial \mathcal{J}_S / \partial \mathbf{q})^T = 0$ and $(\partial \mathcal{J}_A / \partial \mathbf{q})^T$ is computed in the same way as in aerodynamic optimization. Evaluation of the off-diagonal term, $(\partial \mathbf{R}_S / \partial \mathbf{q})^T$, is as described by Kenway *et al.*,²³ where

$$\frac{\partial \mathbf{R}_S}{\partial \mathbf{q}}^T \Psi_S = \frac{\partial \mathbf{f}_A}{\partial \mathbf{q}}^T \frac{\partial \mathbf{f}_S}{\partial \mathbf{f}_A}^T \frac{\partial \mathbf{R}_S}{\partial \mathbf{f}_S}^T \Psi_S. \quad (22)$$

Sensitivities of the aerodynamic forces, \mathbf{f}_A , with respect to \mathbf{q} are computed within the aerodynamic module, whereas $(\partial \mathbf{f}_S / \partial \mathbf{f}_A)^T$ is computed in TACS by analytical differentiation of the force transfer routine.

In (20), $(\partial \mathcal{J}_A / \partial \mathbf{u})^T$ is zero due to the explicit mesh state. Similarly, contributions from the following forces, $(\partial \mathbf{f}_S / \partial \mathbf{u})^T (\partial \mathbf{R}_S / \partial \mathbf{f}_S)^T \Psi_S^{(k)}$, are also zero. The directions of the forces, \mathbf{f}_A and \mathbf{f}_S , now depend explicitly on \mathbf{b}_Δ instead of \mathbf{u} . Sensitivities of the aerodynamic mesh with respect to \mathbf{u} are included in

$$\frac{\partial \mathbf{R}_{M\Delta}}{\partial \mathbf{u}}^T \Psi_{M\Delta} = \frac{\partial \mathbf{u}_A}{\partial \mathbf{u}}^T \frac{\partial \tilde{\mathbf{G}}_{\Delta s}}{\partial \mathbf{u}_A}^T \frac{\partial \mathbf{b}_s}{\partial \tilde{\mathbf{G}}_{\Delta s}}^T \frac{\partial \mathbf{R}_{M\Delta}}{\partial \mathbf{b}_s}^T \Psi_{M\Delta}. \quad (23)$$

The evaluation of $(\partial \mathbf{R}_{M\Delta} / \partial \mathbf{b}_s)^T \Psi_{M\Delta}$ uses existing routines in the aerodynamic module and is analytical. The matrix-vector product involving the sensitivities of the displaced surface control points with respect to the exact displaced surface, $(\partial \mathbf{b}_s / \partial \tilde{\mathbf{G}}_{\Delta s})^T$, is obtained by analytical differentiation of the linear least-squares surface fitting. The last term, $(\partial \mathbf{u}_A / \partial \mathbf{u})^T$, depends on the displacement transfer scheme and is computed analytically in TACS. Equation (20) is solved by the same routines as in structural analysis due to the symmetry of \mathbf{K}_S .

For the mesh adjoint equation given by (21), the aerodynamic mesh state due to structural deflections does not contribute directly to the calculation of \mathcal{J}_S , so $(\partial \mathcal{J}_S / \partial \mathbf{b}_\Delta)^T$ is zero. Furthermore, $(\partial \mathcal{J}_A / \partial \mathbf{b}_\Delta)^T$ and $(\partial \mathbf{R}_A / \partial \mathbf{b}_\Delta)^T \Psi_A$ are both obtained by first differentiating with respect to the aerodynamic volume grid, \mathbf{G} , then completing the chain rule by $(\partial \mathbf{G} / \partial \mathbf{b}_\Delta)^T$. Calculation of the last term,

$$\frac{\partial \mathbf{R}_S}{\partial \mathbf{b}_\Delta}^T \Psi_S = \frac{\partial \mathbf{G}}{\partial \mathbf{b}_\Delta}^T \frac{\partial \mathbf{f}_S}{\partial \mathbf{G}}^T \frac{\partial \mathbf{R}_S}{\partial \mathbf{f}_S}^T \Psi_S, \quad (24)$$

reuses matrix-vector products that are already present in the other terms, with the exception of $(\partial \mathbf{f}_S / \partial \mathbf{G})^T$, which is obtained by analytically differentiating the aerodynamic grid contribution in the surface traction calculation and in the force transfer process. Equation (21) is solved by existing mesh adjoint solution routines in the aerodynamic module.

Block Gauss-Seidel iterations involving (19–21) are repeated until all residual norms drop below a specified tolerance relative to their initial values. Once the adjoint variables are obtained, they are substituted into (18)

for the total gradient. Sensitivities with respect to aerodynamic design variables, \mathbf{v}_A , and structural design variables, \mathbf{v}_S , are reduced to

$$\mathcal{G}_A = \frac{\partial \mathcal{J}^T}{\partial \mathbf{v}_A} + \frac{\partial \mathbf{R}_A^T}{\partial \mathbf{v}_A} \Psi_A \quad \text{and} \quad \mathcal{G}_S = \frac{\partial \mathcal{J}^T}{\partial \mathbf{v}_S} + \frac{\partial \mathbf{R}_S^T}{\partial \mathbf{v}_S} \Psi_S, \quad (25)$$

respectively. Sensitivities with respect to geometric design variables, \mathbf{v}_G , are more involved. For aerodynamic functionals, the terms $(\partial \mathbf{R}_A / \partial \mathbf{v}_G)^T \Psi_A$ and $(\partial \mathcal{J}_A / \partial \mathbf{v}_G)^T$ are both zero. The grid dependence of \mathbf{R}_A and \mathcal{J}_A is expressed through the mesh adjoint term in (18), where

$$\frac{\partial \mathbf{R}_{M\Delta}^T}{\partial \mathbf{v}_G} \Psi_{M\Delta} = \frac{\partial \tilde{\mathbf{G}}_{\Delta s}^T}{\partial \mathbf{v}_G} \frac{\partial \mathbf{b}_s^T}{\partial \tilde{\mathbf{G}}_{\Delta s}} \frac{\partial \mathbf{R}_{M\Delta}^T}{\partial \mathbf{b}_s} \Psi_{M\Delta}. \quad (26)$$

Kenway *et al.*²³ have pointed out that the exact displaced surface, $\tilde{\mathbf{G}}_{\Delta s}$, depends explicitly on \mathbf{v}_G through changes in both the jig shape and the rigid link vectors. This subtle relationship has been included to accurately evaluate $(\partial \tilde{\mathbf{G}}_{\Delta s} / \partial \mathbf{v}_G)^T$ in (26). Calculations involving $(\partial \mathbf{b}_s / \partial \tilde{\mathbf{G}}_{\Delta s})^T$ reuse the routine for the same term in (23). For structural functionals, the sensitivities of \mathbf{R}_S and \mathcal{J}_S with respect to \mathbf{v}_G come from changes in the structural mesh, \mathbf{M}_S , as a result of geometric changes. They are calculated as follows:

$$\frac{\partial \mathbf{R}_S^T}{\partial \mathbf{v}_G} \Psi_S = \left(\frac{\partial \mathbf{M}_S^T}{\partial \mathbf{v}_G} \frac{\partial \mathbf{K}_S^T}{\partial \mathbf{M}_S} \frac{\partial \mathbf{R}_S^T}{\partial \mathbf{K}_S} + \frac{\partial \mathbf{r}^T}{\partial \mathbf{v}_G} \frac{\partial \mathbf{f}_S^T}{\partial \mathbf{r}} \frac{\partial \mathbf{R}_S^T}{\partial \mathbf{f}_S} \right) \Psi_S, \quad (27)$$

$$\frac{\partial \mathcal{J}_S^T}{\partial \mathbf{v}_G} = \frac{\partial \mathbf{M}_S^T}{\partial \mathbf{v}_G} \frac{\partial \mathcal{J}_S^T}{\partial \mathbf{M}_S}, \quad (28)$$

where $(\partial \mathbf{M}_S / \partial \mathbf{v}_G)^T$ involves differentiating (7) for each point on the structural model with respect to the jig shape surface control points. The second term on the right-hand side of (27) captures the effect of changing the rigid link vectors on the force transfer calculations.

VI. Verification and Validation

The main objective of this section is to verify and validate various aspects of the current aerostructural analysis and optimization framework. First, the performance of the force and displacement transfer scheme is analyzed and compared to an existing framework. Then, the aerostructural analysis capability is validated by comparing computational results to experimental data. Finally, a thorough gradient verification test is performed to ensure that the analytical gradients provided to the optimizer are reasonably accurate.

VI.A. Force and Energy Conservation

The main objective of this section to investigate whether the errors associated with fitting the displaced surface, as described in step 3 of Section IV.C on page 9, degrade the performance of the aerostructural solver. Specifically, it is important to ensure that this particular transfer scheme does not hinder the grid convergence characteristics of functionals of interest such as lift and drag. This is an essential consideration in practical application of the optimization framework. To accomplish this goal, an aerostructural analysis on an optimized wing is performed and the resultant forces as well as the work done on the two domains are compared. Then, a grid refinement study on the aerodynamic mesh is performed to demonstrate that a functional of interest becomes independent of the grid resolution within a specific tolerance. The node density of the structural domain is kept constant. A more thorough approach would be to characterize the effects of the structural mesh density on the grid convergence characteristics of the aerodynamic functional of interest. However, that is outside the scope of the present study due to the fact that in most practical applications, the structures are sized for a given structural mesh density.

An important characteristic of a desirable transfer scheme is that it conserves the resulting forces as well as the work done by the aerodynamic and structural nodes at the interface.^{39,40,41,42} The degree to which the current transfer scheme violates this principle is an indication of the error introduced by fitting the displaced surface during an aerostructural analysis. Thus, to fully understand the implications of the fitting step, this error is also monitored as the aerodynamic mesh resolution increases. Furthermore, this error is compared to the results produced by another framework that uses the same transfer scheme, but captures

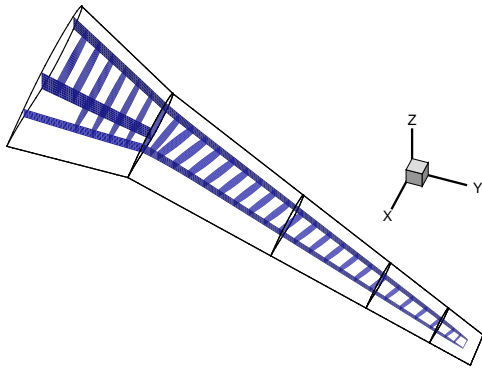


Figure 3: The outer mold line of the initial wing with the structural components inside the wingbox.

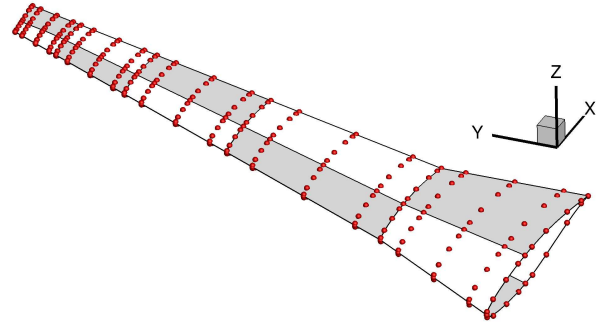


Figure 4: Geometry parameterization shown with the surface patches and control points.

the displacements exactly,⁴³ i.e. without fitting error, so that it preserves the consistency and conservation property from the original transfer scheme.^{24,23} For clarity, this methodology will be referred to as the second framework. Both frameworks use inviscid aerostructural analysis for this study.

To obtain the wing geometry for the analysis involved in this study, an aerostructural optimization is performed to obtain a suitable design. The planform of this design, shown in Figures 3 and 4, is based on the Boeing 737-900 wing. The optimization minimizes the drag under cruise conditions while maintaining the structural integrity of the wing at a $2.5g$ load condition. The cruise Mach number is 0.74 at an altitude of 30,000 feet, while the Mach number for the $2.5g$ load condition is equal to 0.85 at an altitude of 20,000 feet. The wing material is based on the 7075 Aluminum with a Poisson's ratio of 0.33 and Young's modulus of 70GPa. The optimizer is free to change the sectional shape and twist of the wing along the span. However, the thickness-to-chord ratio of the wing is not allowed to reduce by more than 10% of the initial value anywhere along the chord. The optimization is launched with the RAE 2822 airfoil as the initial section. The optimized wing is then used for the purpose of this study using the current framework.

The wing geometry used to perform the mesh refinement studies with the second framework is obtained by performing a similar aerostructural optimization case using the second framework. As a result, this optimized wing differs slightly from the one described above. This is done in part to develop a better understanding of the differences between the two optimized wings that are obtained with the two different frameworks. However, the subtle differences observed in the two optimal designs are not discussed here.

Figure 5 shows the convergence of lift coefficient with increasing grid density and control point resolution obtained from the present framework. Figure 6 shows the drag coefficient in drag counts (10^{-4}). The control points are used to fit every patch on the surface of the wing. The upper and lower surfaces of the wing each have 10 patches, as illustrated in Figure 4. Only the number of chordwise control points is increased because it has the greatest impact on whether or not the airfoil shape is captured correctly by the fitting process. The sequence of aerodynamic grids is obtained by doubling the total number of grid nodes at every level using the B-spline parameterization technique to maintain a consistent distribution of grid nodes. These graphs demonstrate that lift and drag change by less than 1% from the second finest to the finest grid level.

Figure 7 shows the convergence of lift coefficient with increasing grid density and control point resolution obtained from the second framework, which is capable of capturing the displaced surface without fitting error. Figure 8 shows the drag coefficient. Figures 7 and 8 show the same convergence trends observed from the results obtained by the present framework. This means that the fitting error introduced during the transfer process does not hinder the convergence of aerodynamic functionals of interest.

To further support the above observations, it is necessary to quantify the transfer error in force and energy conservation. Accuracy of the force transfer can be assessed by how well the resultant forces are conserved between the aerodynamic and structural domains during transfer. Moreover, if there is an error, it must decrease with grid refinement. The same comparison is done for the second framework, which has no fitting error, as a benchmark. Figure 9 shows the variation of the error in all directions for three control point densities with increasing grid resolution. In addition, the error produced by the second framework is shown on the same plot. Note that the error is nonzero for both frameworks possibly due to the fact that the structural solver uses a different force integration scheme than the aerodynamic solver. Hence the error

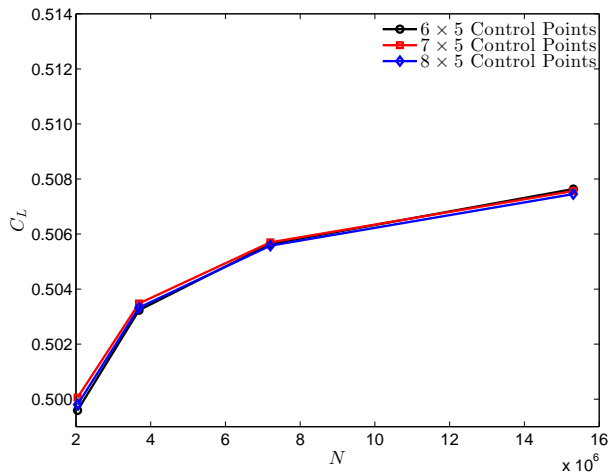


Figure 5: Convergence of lift coefficient for increasing grid density and control point resolution.

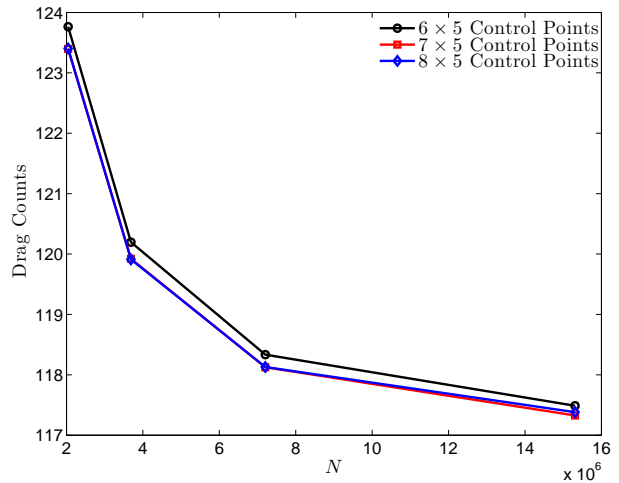


Figure 6: Convergence of drag coefficient for increasing grid density and control point resolution.

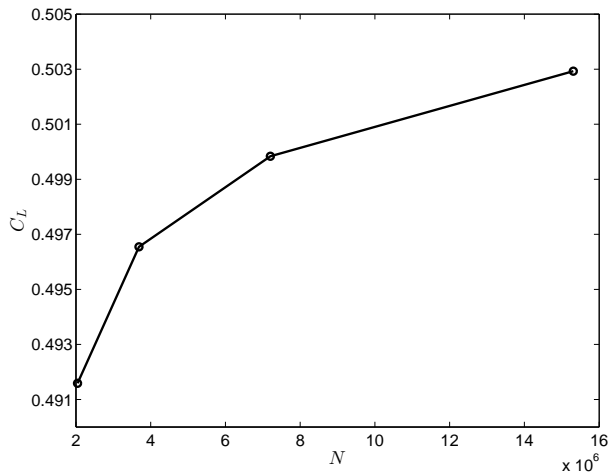


Figure 7: Convergence of lift coefficient for increasing grid density obtained from the second framework.

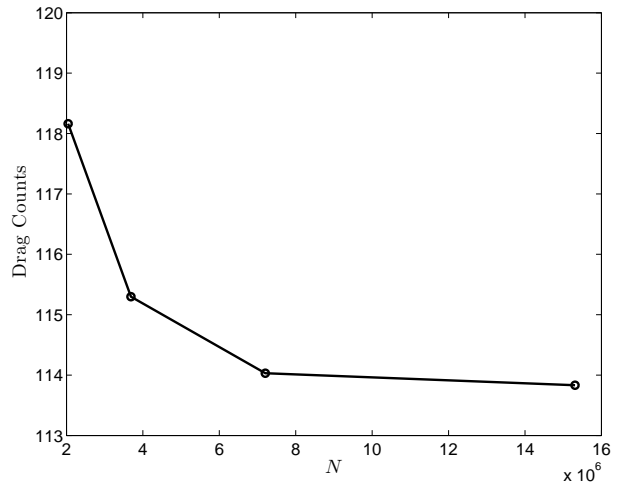


Figure 8: Convergence of drag coefficient for increasing grid density obtained from the second framework.

appears to be independent of the number of surface control points. However, it is clear that in all cases, the error in force transfer introduced by the current framework is similar to the error produced by the second framework.

A similar assessment is conducted for energy conservation, which requires that the work done on the aerodynamic and structural sides of the interface are equal. Figure 10 shows the variation of the error in the energy transfer for various surface control point densities with increasing mesh resolution. Moreover, the same error is shown on the same plot for the second framework. The error in Figure 10 is due to the force transfer error in Figure 9 and the error in the displacement transfer due to surface fitting. It is evident that although the current force and displacement transfer scheme is not conservative, it is producing a similar or lower error in comparison to the framework that captures the displacements exactly. Therefore, it is safe to conclude that the error introduced by fitting has a minor impact on the accuracy of the transfer.

VI.B. Validation Based on the HIRENASD Wing

The High REynolds Number Aero-Structural Dynamics (HIRENASD) Project was initiated to provide experimental aeroelastic data for a large transport wing-body configuration.^{44,45,46} Figure 11 provides details about the geometry and wind tunnel assembly of the HIRENASD wing. The main objective of this

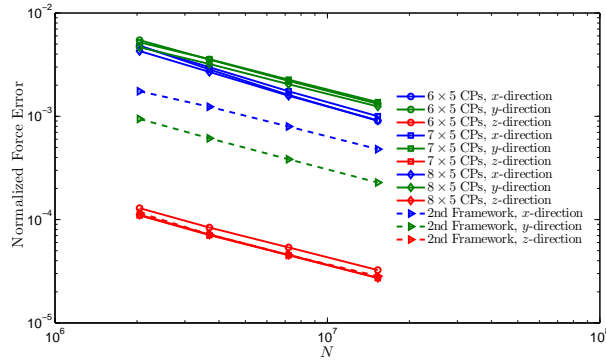


Figure 9: Variation of error in the force transferred in all directions with increasing control point (CP) density and mesh resolution for the two transfer schemes.

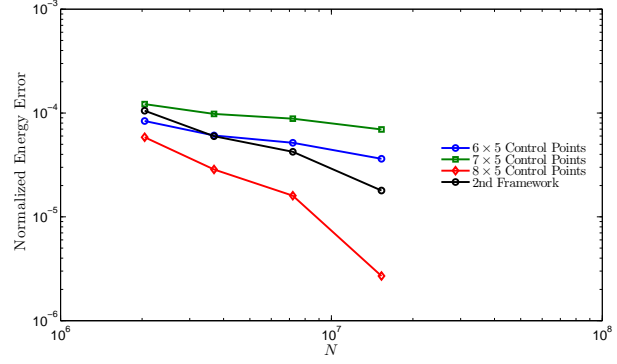


Figure 10: Variation of error in the energy transferred with increasing control point density and mesh resolution for the two transfer schemes.

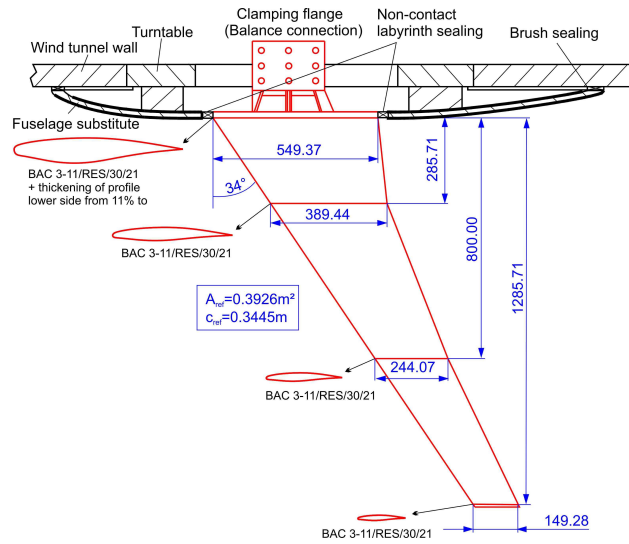


Figure 11: Geometric planform and wind tunnel setup of the HIRENASD wing model.^a

section is to compare static aeroelastic computational results obtained using the present framework with the HIRENASD experimental data.

The test condition Mach number, angle of attack, and Reynolds number are 0.80, 1.5°, and 7.0×10^6 , respectively. An aerostructural analysis is performed to obtain the computational results. The one-equation Spalart-Allmaras turbulence model is used to model the turbulent flow in this test case. Osusky and Zingg³⁶ provide comprehensive details of the Reynolds-Averaged-Navier-Stokes flow solver.

A multiblock structured grid is used for the aerodynamic solver with 3,548,095 nodes. The average y^+ value is equal to 0.24. The finite-element model provided by the HIRENASD project contained solid elements. However, the structural solver, TACS, accepts MITC shell elements only. Furthermore, the current structural model does not include the leading and trailing edges. Thus, an effort has been made to ensure that the structural finite-element model used in this analysis most closely represents the original structure of the HIRENASD wing. This finite-element model for the structures has approximately 38,000 second-order MITC shell elements.

Figure 12 provides a comparison of the computational static aerostructural results with the experimental data. Specifically, the contours of pressure coefficient at various spanwise locations on the surface of the wing are being compared to experimental results. In addition, the rigid-body results (where there are no

^aUsed with permission from: <http://heinrich.lufmech.rwth-aachen.de/en/windtunnel-assembly>

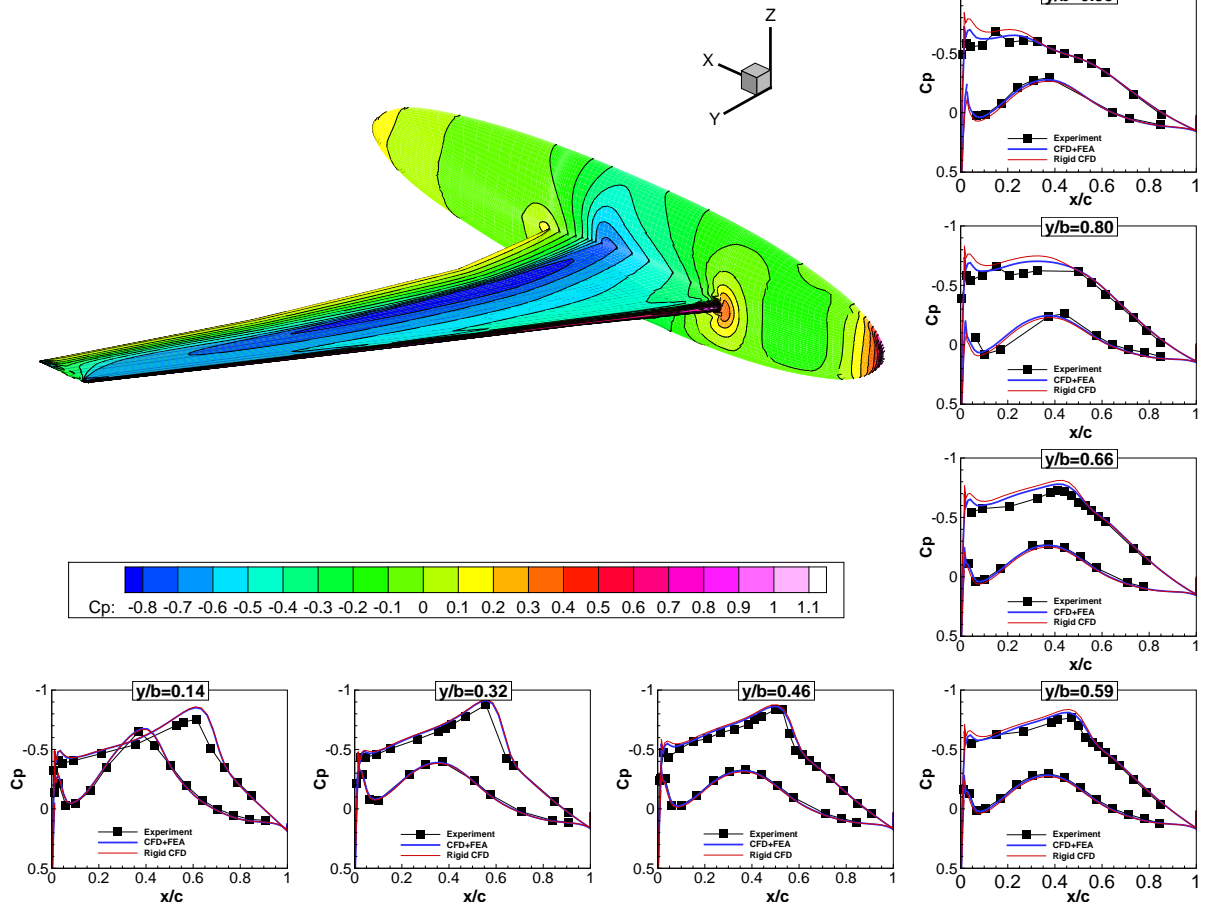


Figure 12: Comparison of experimental and computational pressure coefficient results for the HIRENASD wing geometry. The experimental, static aeroelastic, and rigid-wing results are shown for each spanwise station.

structural deflections) are provided for reference. Figure 12 demonstrates that the static aerostructural results obtained from the present framework compare well with the experimental data.

VI.C. Gradient Verification

This section compares the gradient values by the coupled adjoint method with second-order finite-difference approximations. The geometry in Figure 3 and 4 is again used. The aerodynamic mesh has 2,044,056 nodes and is divided into 192 blocks. Each block is parameterized by $6 \times 5 \times 9$ B-spline control points. The wing structure has 2 main spars and 30 ribs, as shown in Figure 3. The corresponding finite-element mesh consists of 30,473 second-order MITC shell elements and 174,204 degrees of freedom. The functionals considered include the drag and lift forces, as well as the KS functions for structural failure. Due to the nature of the stress distribution, three KS functions with an aggregation parameter of 30.0 are used to monitor structural failure in the 1) ribs and spars, 2) top skin, and 3) bottom skin. All KS functions incorporate a safety factor of 2.0. The design variables include a uniform thickness value for all structural members, AoA, and the span. The study is conducted at a Mach number of 0.74 at an altitude of 30,000 feet, with an AoA of 3.0° . An initial thickness of 5mm is used for all structural members. The material used for the structures is based on the 7075 Aluminum with a Poisson's ratio of 0.33 and Young's modulus of 70GPa. Figure 13 plots the relative error between the calculated gradient values and the finite-difference approximations for different step sizes. The largest minimum relative error is on the order of 10^{-7} , but the majority of the gradient values have a minimum relative error on the order of 10^{-8} . This shows excellent agreement between the

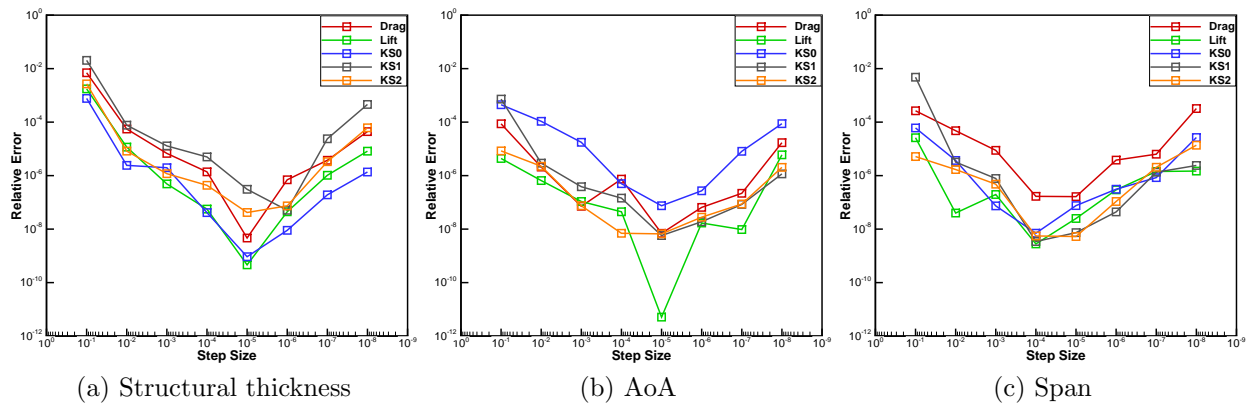


Figure 13: Relative error in functional and constraint gradients between the adjoint method and finite-differences.

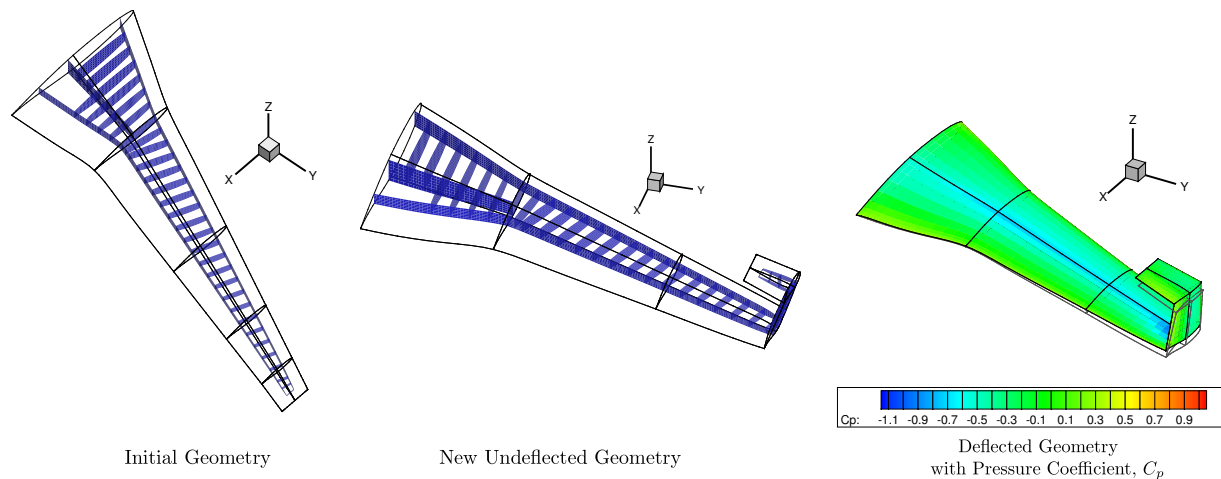


Figure 14: Illustration of substantial geometry changes achieved by the integrated geometry parameterization and mesh movement. The right-most figure shows the new geometry and its Mach contour under structural deflection, which is superimposed on the undeformed geometry

computed gradients and the finite-difference approximations.

VII. Application to Aerostructural Analysis and Optimization

This section demonstrates the capabilities of the current aerostructural analysis and optimization framework through its application to two cases. The first is an aerostructural analysis of a C-wing geometry in transonic flow. This case shows that the present framework is able to deform a planar wing to a complex C-wing geometry using the integrated mesh movement scheme and perform an analysis successfully. The second case investigates the fundamental tradeoff between weight and drag that is involved in the design of conventional wings. In the context of aircraft design, weight and drag are competing objectives. The results demonstrate that the current framework is able to capture this tradeoff by manipulating the quarter-chord sweep angle of a planar wing.

VII.A. Analysis of a C-Wing

To demonstrate the capability of the integrated geometry parameterization and mesh movement to handle large shape changes, a simple initial wing geometry is deformed into a user-specified C-wing geometry using the integrated methodology, and aerostructural analysis based on the Euler equations is performed on the resulting geometry. The initial geometry shown on the left in Figure 14 is planar, swept back, and tapered

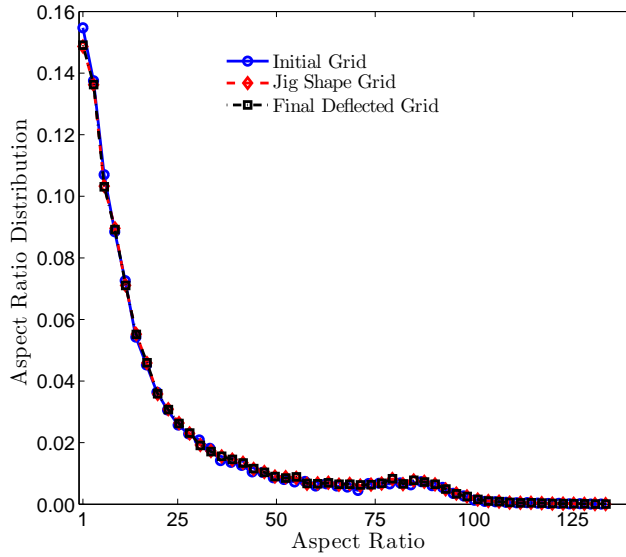


Figure 15: Cell aspect ratio distribution of the aerodynamic grids for the initial, undeflected jig, and final deflected shapes.

with the RAE 2822 airfoil. The aerodynamic grid, which is not shown, consists of 193,536 nodes and 112 blocks. Each block is parameterized by $6 \times 6 \times 6$ control points. The surface geometry consists of 20 surface patches, which leads to 30 surface control points in the spanwise direction and 12 in the chordwise direction. The structural model has 30,473 second-order MITC shell elements and it is shown in blue with the initial geometry and the undeflected C-wing. It is evident that surface-based FFD successfully moved the internal structure during the initial shape change without distorting the individual components.

The aerostructural analysis of the C-wing uses a Mach number of 0.785 at an AoA of 0.0° , and it assumes an altitude of 35,000 feet. The material used for the structures is based on the 7075 Aluminum with a Poisson's ratio of 0.33 and Young's modulus of 70GPa. All structural components in the wing have a thickness of 7.5mm. These parameters are chosen to induce a realistic structural deflection in the wing, which is observed in the final geometry shown on the right in Figure 14. The aerostructural analysis converged by 7 orders of magnitude in 11 nonlinear block Gauss-Seidel iterations, requiring a total solution time of approximately 11 minutes with 64 processors. Figure 15 shows that the aspect ratio distribution has not changed significantly from the initial grid. Thus, the quality of the grid generated around the initial geometry shown in Figure 14 has been preserved. This study demonstrates that the geometry parameterization and mesh movement algorithm has sufficient flexibility and robustness to be extended to applications involving exploratory design optimization, as well as gradient-based multi-start optimization.⁴⁸

VII.B. Inviscid Transonic Wing Sweep Optimization

There is a fundamental tradeoff between weight and drag in the design of aircraft wings. For instance, at transonic speeds, increasing the quarter-chord sweep angle of a wing reduces the wave drag, but the corresponding increase in the weight may overshadow the drag benefit in such a way that the resulting range is reduced. The main objective of this section is to investigate whether the current framework is able to capture this important tradeoff correctly in the context of an aerostructural optimization of a conventional planar wing.

The choice of the objective function in optimization influences the final optimized design. In the practical design of aircraft wings, the objective is carefully chosen based on the design requirements for a particular aircraft. However, for the purpose of this study, only the tradeoff between weight and drag is of interest. For this reason, the objective function has the form

$$\mathcal{J} = \beta \frac{\mathcal{D}}{\mathcal{D}_0} + (1 - \beta) \frac{\mathcal{W}}{\mathcal{W}_0}, \quad (29)$$

where β is a parameter between zero and unity, \mathcal{D} is the inviscid drag of the wing in cruise, \mathcal{W} is the

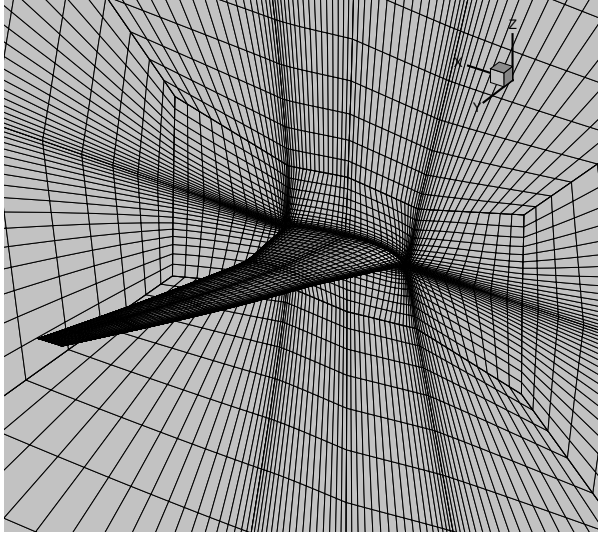


Figure 16: Grid resolution of the surface and symmetry plane for the fine optimization mesh.

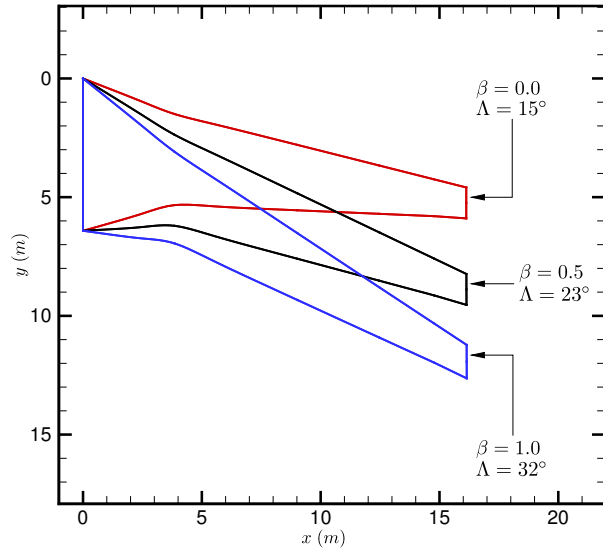


Figure 17: The planforms for the three wings show that the optimal sweep angle, Λ , increases with increasing β , i.e. increasing emphasis on drag.

calculated weight of the wing satisfying the structural failure constraints at a $2.5g$ load condition, and \mathcal{D}_0 and \mathcal{W}_0 are the respective initial values. As β is varied from zero to unity, the emphasis on drag in the objective function is increased while reducing the emphasis on weight. Three values for β have been chosen: 0.0, 0.5, and 1.0.

There are two lift constraints; one corresponds to the cruise load condition, the other to the $2.5g$ load condition. The cruise Mach number is 0.74 at an altitude of 30,000 feet while the Mach number for the $2.5g$ load condition is 0.85 at an altitude of 20,000 feet. Since the weight of the wing is a function of the structural thickness values, it changes over the course of the optimization. The total weight of the aircraft is assumed to be equal to the computed weight of the wing plus a fixed weight of 785,000N. This fixed weight is estimated based on the maximum takeoff weight of a Boeing 737-900 discounted by the approximate wing weight. The approximate wing weight is equal to 7% of the maximum takeoff weight.

The stresses on the wing due to the aerodynamic loads at the $2.5g$ load condition are aggregated using three KS functions with an aggregation parameter of 30.0. There is one KS function for the ribs and spars, one for the top skin, and one for the bottom skin of the wing. These KS functions are constrained to ensure structural integrity of the wing. The material is based on the 7075 Aluminum with a Poisson's ratio of 0.33 and Young's modulus of 70GPa. The yield stress is 434MPa, and a safety factor of two is applied. The reduction in the thickness of the wing is limited to 10% of the initial value.

The aerostructural optimizations are initiated with a planar wing geometry based on the Boeing 737-900 planform. Figure 3 shows the layout of the wing and the structures inside the wingbox. Initially, a coarse CFD grid is used with 193,536 nodes and 112 blocks. Once the optimizer satisfies the nonlinear constraints on this coarse mesh, the optimization is restarted using a finer mesh with 653,184 nodes and 112 blocks. Figure 16 shows the grid resolution of the surface and symmetry plane for the fine mesh. Each block is parameterized with $6 \times 6 \times 6$ control points. The upper and lower surfaces of the wing are parameterized with 10 B-spline surface patches. The structures mesh has 30,473 second-order MITC shell elements.

The initial airfoil is the RAE 2822. The optimizer is free to change the tip twist and section shape at 16 spanwise stations in addition to the quarter-chord sweep angle. Each spanwise station is parameterized by 24 control points, 14 of which are design variables. The sweep angle is varied in such a way that the initial span of the wing is maintained. The total number of geometric design variables is equal to 226. Furthermore, there are a total of 156 structural design variables which determine the thickness of structural components inside the wingbox. Finally, there are two angle of attack design variables; one for cruise, the other for the $2.5g$ load condition.

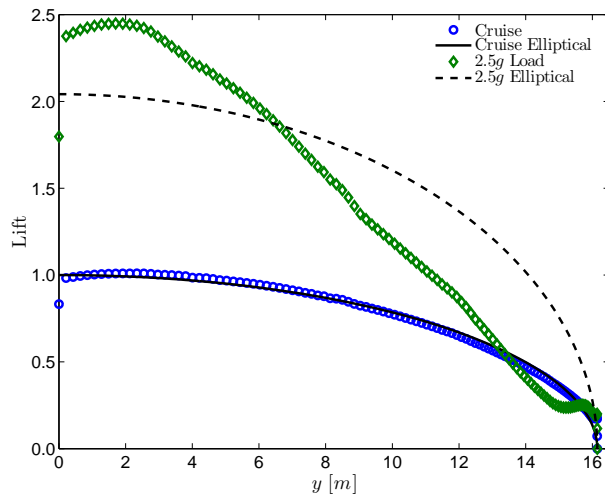


Figure 18: Cruise and 2.5g load distributions along the span of the wing for the $\beta = 1.0$ case.

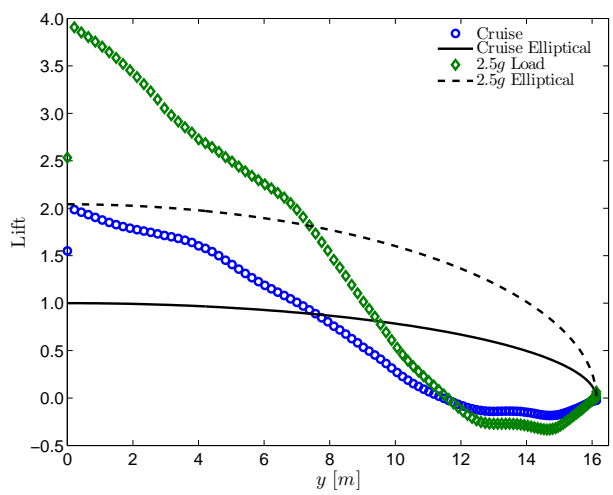


Figure 19: Cruise and 2.5g load distributions along the span of the wing for the $\beta = 0.0$ case.

As β is varied from 0.0 to 1.0, i.e. as more emphasis is placed on drag and less on weight, the optimizer should take advantage of the available freedom to increase the sweep angle of the wing in order to reduce drag. As a result, the sweep angles of the optimized designs should increase with increasing β . Figure 17 shows the planform of the three optimized wings. It is clear that the optimizer has produced the expected trend. This means that the present aerostructural optimization framework is capable of capturing the tradeoff between weight and drag. Furthermore, it is interesting to note that the quarter-chord sweep angle of the optimized wing for the $\beta = 0.5$ case is equal to 23° , close to that of the Boeing 737-900, which is 25° .

Figures 18 and 19 show the spanwise lift distributions at the cruise and 2.5g load conditions for the $\beta = 1.0$ and $\beta = 0.0$ cases, respectively. All lift values have been normalized by the elliptical lift at the root of the wing for cruise. For the $\beta = 1.0$ case, the cruise lift distribution closely follows the elliptical load, while the 2.5g spanwise lift distribution is much more triangular in comparison to cruise. This means that the optimizer is taking advantage of aeroelastic tailoring to minimize inviscid drag in cruise both by maintaining an optimal lift distribution and increasing the quarter-chord sweep angle. This is done while maintaining the structural integrity of the wing at the 2.5g load condition by reducing the tip loading. It is also insightful to examine the $\beta = 0.0$ case. With $\beta = 0.0$, the lift distributions for both the cruise and 2.5g load conditions are triangular because the objective function is simply the normalized weight of the wing. At the 2.5g load condition, the tip loading is in fact negative allowing for a significant reduction in the root bending moment.

The $\beta = 0.0$ case is particularly difficult to converge. With $\beta = 0.0$, the objective function is equal to the normalized weight of the wing. Since the quarter-chord sweep angle is free to change, the optimizer reduces the sweep as much as possible in order to take advantage of the corresponding reduction in structural weight. This leads to designs that have strong shock waves on the upper and lower surfaces of the wing. As a result, the $\beta = 0.0$ case presented in this paper is not converged as deeply as the rest of the cases. The highest nonlinear constraint violation for this case is 5.3×10^{-4} , almost two orders of magnitude larger than the rest of the cases. Therefore, the reader should not attach too much significance to the value of the quarter-chord sweep angle for this case. However, this does not skew the main conclusions because the expected trends have indeed been recovered.

Figures 20 and 21 show the optimized thickness distribution of structural components for the $\beta = 0.0$ and $\beta = 1.0$ cases, respectively. The optimizer has increased the thickness inboard in both cases. Furthermore, it is clear that the $\beta = 0.0$ has lighter components in comparison to the $\beta = 1.0$ case. Although only a single critical structural load condition has been considered in all cases, these results show that at least some of the correct trends in the structural sizing of the wings have been captured.

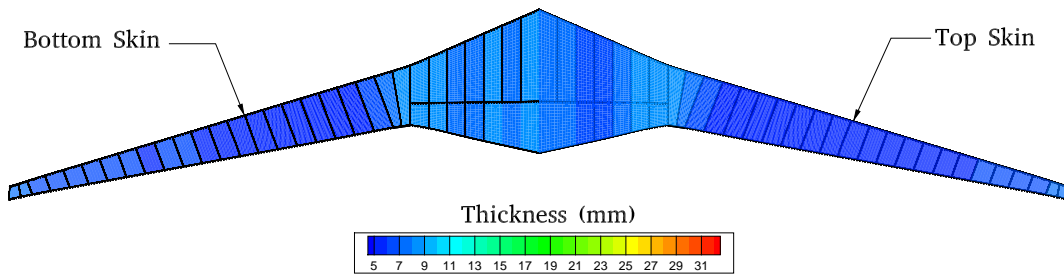


Figure 20: The optimized thickness distribution of structural components for the $\beta = 0.0$ case.

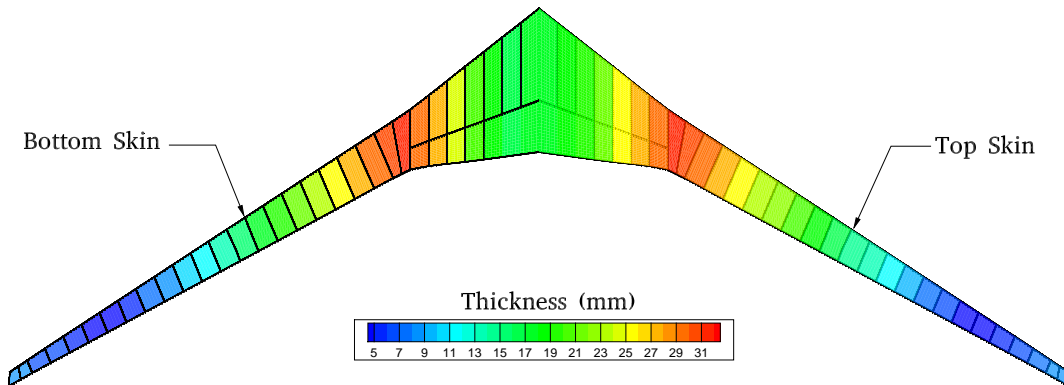


Figure 21: The optimized thickness distribution of structural components for the $\beta = 1.0$ case.

VIII. Conclusion

This paper describes and demonstrates the application of the integrated geometry parameterization and mesh movement algorithm of Hicken and Zingg¹⁶ to high-fidelity aerostructural optimization problems. This approach analytically describes the undeflected geometry and the flying shape of the design using B-spline surface control points. It has numerous advantages compared to other CAD-free geometry parameterization techniques which operate on discrete geometry representations. The geometry parameterization is tightly integrated with an efficient and robust mesh movement algorithm that allows high quality computational grids to be obtained for the aerodynamic domain in response to any shape changes. The present framework includes the introduction of a novel structural mesh movement strategy. A three-field formulation has also been proposed to simplify the analysis and the coupled adjoint problem, where B-spline control point coordinates are treated as explicit state variables. Implementation details on the aerostructural solution procedure and the coupled adjoint calculations have also been provided.

The accuracy of the described framework is validated via several analysis and optimization studies. First, effects of the surface fitting during displacement transfer have been quantified for both analysis and optimization. The study shows that although the B-spline surface does not exactly capture the displacements described by the original transfer scheme,^{22,23,24} it does not affect the grid convergence of functional values. The same study further shows that during an analysis, forces and energy are conserved to approximately the same degree with and without the displaced surface fitting. In the second study, the present framework has accurately modeled static aerostructural experimental data from the HIRENASD project. A further study verifies the coupled adjoint gradient calculation through comparison with finite-difference approximations using varying step sizes. The minimum relative error is on the order of 10^{-8} . Based on the above studies, it can be concluded that the present framework is sufficiently accurate to be used in practical aerostructural design problems.

Two examples are included to show how the present framework performs in aerostructural applications. The first case is the analysis of a C-wing that is generated from a simpler geometry using the integrated geometry parameterization and mesh movement methodology. This has demonstrated the robustness of the framework in the presence of aggressive shape changes. The framework is also applied in a wing sweep optimization study involving a realistic number of design variables. The results of this study accurately

reflect the fundamental tradeoff between weight and drag in aerostructural design problems.

Future development will include the application of the present framework to more practical design problems and exploratory optimization studies. The gradient calculations will be extended to incorporate aerostructural RANS analysis. More efficient and robust aerostructural solution strategies, such as monolithic methods, will be sought to further improve the feasibility and convenience of this framework as a practical design tool.

Acknowledgments

The authors would like to acknowledge Prof. J. R. R. A. Martins at the University of Michigan, Ann Arbor for sharing his framework for the purpose of constructing our methodology. The authors are also grateful for the funding provided by Zonta International Amelia Earhart Fellowships, the Ontario Graduate Scholarship, and the National Sciences and Engineering Research Council Postgraduate Scholarship. Computations were performed on the GPC supercomputer at the SciNet HPC Consortium. SciNet is funded by the Canada Foundation for Innovation under the auspices of Compute Canada, the Government of Ontario, Ontario Research fund - Research Excellence, and the University of Toronto.

References

- ¹“Annual Energy Outlook with Projections to 2035,” Online: <http://www.eia.gov/forecasts/aeo/>, April 2011, U.S. Energy Information Administration.
- ²“Energy and Financial Markets: What Drives Crude Oil Prices,” Online: <http://www.eia.gov/finance/markets/>, December 2011, U.S. Energy Information Administration.
- ³“Climate change 2007: IPCC synthesis report,” Online: http://www.ipcc.ch/publications_and_data/publications_ipcc_fourth_assessment_report_synthesis_report.htm, November 2007.
- ⁴“Overview of NASA’s Environmentally Responsible Aviation (ERA) Project,” 48th AIAA Aerospace Sciences Meeting, January 2010.
- ⁵Torenbeek, E. and Deconinck, H., “Innovative configurations and advanced concepts for future civil aircraft,” Lecture Series, June 2006.
- ⁶Zingg, D. W., Nemec, M., and Pulliam, T. H., “A comparative evaluation of genetic and gradient-based algorithms applied to aerodynamic optimization,” *Revue européenne de mécanique numérique*, Vol. 17, No. 1-2, March 2008, pp. 103–126.
- ⁷Pironneau, O., “On optimum design in fluid mechanics,” *Journal of Fluid Mechanics*, Vol. 64, No. 1, 1974, pp. 97–110.
- ⁸Jameson, A., “Aerodynamic design via control theory,” *Journal of Scientific Computing*, Vol. 3, No. 3, 1988, pp. 233–260.
- ⁹Hicken, J. E. and Zingg, D. W., “Induced-Drag Minimization of Nonplanar Geometries Based on the Euler Equations,” *AIAA J.*, Vol. 48, No. 11, 2010, pp. 2564–2575.
- ¹⁰Gagnon, H. and Zingg, D. W., “High-fidelity Aerodynamic Shape Optimization of Unconventional Aircraft through Axial Deformation,” *AIAA SciTech, 52nd Aerospace Sciences Meeting*, No. 2014-0908, National Harbor, Maryland, January 2014.
- ¹¹Leoviriyakit, K., Kim, S., and Jameson, A., “Aero-Structural Wing Planform Optimization Using the Navier-Stokes Equations,” *10th AIAA/ISSMO Multidisciplinary Analysis and Optimization Conference*, No. AIAA-2004-4479, Albany, New York, Aug 30 - Sept 1 2004.
- ¹²Jameson, A., Leoviriyakit, K., , and Shankaran, S., “Multi-point Aero-Structural Optimization of Wings Including Planform Variables,” *45th Aerospace Sciences Meeting and Exhibit*, No. AIAA-2007-0000, Reno, Nevada, January 2007.
- ¹³Reist, T. A., , and Zingg, D. W., “Aerodynamic Shape Optimization of a Blended-Wing-Body Regional Transport for a Short Range Mission,” *31st AIAA Applied Aerodynamics Conference*, No. 2013-2414, San Diego, CA, June 2013.
- ¹⁴Lyu, Z. and Martins, J. R. R. A., “Aerodynamic Shape Optimization Studies of a Blended-Wing-Body Aircraft,” *Journal of Aircraft*, Vol. 51, No. 5, 2014, pp. 1604–1617.
- ¹⁵Reuther, J. J., Alonso, J. J., Martins, J. R. R. A., and Smith, S. C., “A Coupled Aero-Structural Optimization Method For Complete Aircraft Configurations,” *AIAA 37th Aerospace Sciences Meeting*, 1999, pp. 99–0187.
- ¹⁶Hicken, J. E. and Zingg, D. W., “Aerodynamic Optimization Algorithm with Integrated Geometry Parameterization and Mesh Movement,” *AIAA J.*, Vol. 48, No. 2, 2010, pp. 400–413.
- ¹⁷Gagnon, H. and Zingg, D. W., “Two-Level Free-Form Deformation for High-Fidelity Aerodynamic Shape Optimization,” *12th AIAA Aviation Technology, Integration, and Operations (ATIO) Conference and 14th AIAA/ISSM*, No. 2012-5447, Indianapolis, Indiana, September 2012.
- ¹⁸Kenway, G. K. W., Kennedy, G. J., and Martins, J. R. R. A., “A CAD-Free Approach to High-Fidelity Aerostructural Optimization,” *Proceedings of the 13th AIAA/ISSMO Multidisciplinary Analysis Optimization Conference*, Fort Worth, TX, September 2010, AIAA 2010-9231.
- ¹⁹Maute, K., Nikbay, M., and Farhat, C., “Coupled Analytical Sensitivity Analysis and Optimization of Three-Dimensional Nonlinear Aeroelastic Systems,” *AIAA J.*, Vol. 39, No. 11, 2001, pp. 2051–2061.
- ²⁰Barcelos, M. and Maute, K., “Aeroelastic design optimization for laminar and turbulent flows,” *Computer Methods in Applied Mechanics and Engineering*, Vol. 197, 2008, pp. 1813–1832.
- ²¹Martins, J. R. R. A., Alonso, J. J., and Reuther, J. J., “High-Fidelity Aerostructural Design Optimization of a Supersonic Business Jet,” *J. Aircraft*, Vol. 41, No. 3, 2004, pp. 523–530.

- ²²Martins, J. R. R. A., Alonso, J. J., and Reuther, J. J., “A Coupled-Adjoint Sensitivity Analysis Method for High-Fidelity Aero-Structural Design,” *Optimization and Engineering*, Vol. 6, 2005, pp. 33–62.
- ²³Kenway, G. K. W., Kennedy, G. J., and Martins, J. R. R. A., “Scalable Parallel Approach for High-Fidelity Steady-State Aeroelastic Analysis and Adjoint Derivative Computations,” *AIAA Journal*, Vol. 52, 2014, pp. 935–951.
- ²⁴Kenway, G. K. W., Kennedy, G. J., and Martins, J. R. R. A., “Multipoint High-Fidelity Aerostructural Optimization of a Transport Aircraft Configuration,” *Journal of Aircraft*, Vol. 51, 2014, pp. 144–160.
- ²⁵Kenway, G. K. W., Kennedy, G. J., and Martins, J. R. R. A., “Aerostructural optimization of the Common Research Model configuration,” *15th AIAA/ISSMO Multidisciplinary Analysis and Optimization Conference*, Atlanta, GA, June 2014.
- ²⁶Osusky, L. and Zingg, D. W., “A Novel Aerodynamic Shape Optimization Approach for Three-Dimensional Turbulent Flows,” *50th AIAA Aerospace Science Meeting including the New Horizons Forum and Aerospace Exposition*, No. AIAA-2012-0058, Nashville, Tennessee, U.S.A., January 2012.
- ²⁷Gill, P. E., Murray, W., Michael, and Saunders, M. A., “SNOPT: An SQP Algorithm For Large-Scale Constrained Optimization,” *SIAM Journal on Optimization*, Vol. 12, 1997, pp. 979–1006.
- ²⁸Perez, R. E., Jansen, P. W., and Martins, J. R. R. A., “pyOpt: A Python-Based Object-Oriented Framework for Nonlinear Constrained Optimization,” *Structures and Multidisciplinary Optimization*, Vol. 45, No. 1, 2012, pp. 101–118.
- ²⁹Wrenn, G. A., “An Indirect Method for Numerical Optimization Using the Kreisselmeier–Steinhauser Function,” , No. CR-4220, 1989.
- ³⁰Kennedy, G. J. and Martins, J. R. R. A., “Parallel Solution Methods for Aerostructural Analysis and Design Optimization,” *13th AIAA/ISSMO Multidisciplinary Analysis Optimization Conference*, No. AIAA-2010-9308, Fort Worth, Texas, September 2010.
- ³¹Poon, N. M. K. and Martins, J. R. R. A., “An Adaptive Approach to Constraint Aggregation Using Adjoint Sensitivity Analysis,” *Structural and Multidisciplinary Optimization*, Vol. 30, No. 1, 2007, pp. 61–73.
- ³²Balay, S., Gropp, W. D., McInnes, L. C., and Smith, B. F., “Efficient Management of Parallelism in Object Oriented Numerical Software Libraries,” *Modern Software Tools in Scientific Computing*, edited by E. Arge, A. M. Bruaset, and H. P. Langtangen, Birkhäuser Press, 1997, pp. 163–202.
- ³³Sederberg, T. W. and Parry, S. R., “Free-form deformation of solid geometric models,” *SIGGRAPH '86 Proceedings of the 13th Annual Conference on Computer Graphics and Interactive Techniques*, Dallas, Texas, August 1986, pp. 151–160.
- ³⁴Nocedal, J. and Wright, S. J., *Numerical Optimization*, Springer, New York, 2nd ed., 2006.
- ³⁵Hicken, J. E. and Zingg, D. W., “Parallel Newton-Krylov Solver for the Euler Equations Discretized Using Simultaneous-Approximation Terms,” *AIAA J.*, Vol. 46, No. 11, 2008, pp. 2773–2786.
- ³⁶Osusky, M. and Zingg, D. W., “Parallel Newton-Krylov-Schur Solver for the Navier-Stokes Equations Discretized Using Summation-By-Parts Operators,” *AIAA Journal*, Vol. 51, No. 12, 2013, pp. 2833–2851.
- ³⁷Kennedy, G. J. and Martins, J. R. R. A., “A parallel finite-element framework for large-scale gradient-based design optimization of high-performance structures,” *Finite Elements in Analysis and Design*, Vol. 87, September 2014, pp. 56–73.
- ³⁸Irons, B. M. and Tuck, R. C., “A version of the Aitken accelerator for computer iteration,” *International Journal for Numerical Methods in Engineering*, Vol. 1, No. 3, 1969, pp. 275–277.
- ³⁹Farhat, C., Lesoinne, M., and LeTallec, P., “Load and motion transfer algorithms for fluid/structure interaction problems with non-matching discrete interfaces: Momentum and energy conservation, optimal discretization and application to aeroelasticity,” *Comp. Meth. Appl. Mech. Eng.*, Vol. 157, 1996, pp. 95–114.
- ⁴⁰Brown, S. A., “Displacement Extrapolation for CFD+CSM Aeroelastic Analysis,” *Proceedings of the 35th AIAA Aerospace Sciences Meeting, Reno, NV*, 1997, AIAA 1997-1090.
- ⁴¹Ahrem, R., Beckert, A., and Wendland, H., “A new multivariate interpolation method for large-scale spatial coupling problems in aeroelasticity,” *the Proceedings to Int. Forum on Aeroelasticity and Structural Dynamics*, 2005.
- ⁴²Deboer, A., Vanzuijlen, A., and Bijl, H., “Comparison of conservative and consistent approaches for the coupling of non-matching meshes,” *Computer Methods in Applied Mechanics and Engineering*, Vol. 197, No. 49-50, Sept. 2008, pp. 4284–4297.
- ⁴³Leung, T. M., Zhang, J., Kenway, G. K. W., Kennedy, G. J., Wang, X., Zingg, D. W., and Martins, J. R. R. A., “Aerostructural Optimization Using a Coupled-Adjoint Approach,” *Canadian Aeronautics and Space Institute 60th Aeronautics and Annual General Meeting*, Toronto, Ontario, May 2013.
- ⁴⁴Ballmann, J., Dafnis, A., Braun, C., Korsch, H., Reimerdes, H. G., and Olivier, H., “The HIRENASD Project: High Reynolds Number Aerostructural Dynamics Experiments in the European Transonic Windtunnel (ETW),” 2006.
- ⁴⁵Ballmann, J., Dafnis, A., Korsch, H., Buxel, C., Reimerdes, H. G., Brakhage, K. H., Olivier, H., Braun, C., Baars, A., and Boucke, A., “Experimental Analysis of High Reynolds Number Aero-Structural Dynamics in ETW,” January 2008.
- ⁴⁶Ballmann, J., Boucke, A., Dickopp, C., and Reimer, L., “Results of Dynamic Experiments in the HIRENASD Project and Analysis of Observed Unsteady Processes,” January 2009.
- ⁴⁷Harris, C. D., “NASA Supercritical Airfoils,” Tech. Rep. 2969, NASA, March 1990.
- ⁴⁸Chernukhin, O. and Zingg, D. W., “Multimodality and Global Optimization in Aerodynamic Design,” *AIAA J.*, Vol. 51, No. 6, 2013, pp. 1342–1354.